Materials Science and Engineering R 44 (2004) 45–89

R Reports: A Review Journal

www.elsevier.com/locate/mser

Available online at www.sciencedirect.com

SCIENCE DIRECT®

Bulk metallic glasses

W.H. Wang[a], C. Dong[b], C.H. Shek[c,*]

[a]*Institute of Physics, Chinese Academy of Science, Beijing, PR China*

[b]*State Key Laboratory of Materials Modification and Department of Materials Engineering, Dalian University of Technology, Dalian 116024, PR China*

[c]*Department of Physics and Materials Science, City University of Hong Kong, Kowloon Tong, Hong Kong, PR China*

Received 2 February 2004; accepted 4 March 2004

Available online 10 May 2004

Abstract

Amorphous alloys were first developed over 40 years ago and found applications as magnetic core or reinforcement added to other materials. The scope of applications is limited due to the small thickness in the region of only tens of microns. The research effort in the past two decades, mainly pioneered by a Japanese- and a US-group of scientists, has substantially relaxed this size constrain. Some bulk metallic glasses can have tensile strength up to 3000 MPa with good corrosion resistance, reasonable toughness, low internal friction and good processability. Bulk metallic glasses are now being used in consumer electronic industries, sporting goods industries, etc. In this paper, the authors reviewed the recent development of new alloy systems of bulk metallic glasses. The properties and processing technologies relevant to the industrial applications of these alloys are also discussed here. The behaviors of bulk metallic glasses under extreme conditions such as high pressure and low temperature are especially addressed in this review. In order that the scope of applications can be broadened, the understanding of the glass-forming criteria is important for the design of new alloy systems and also the processing techniques.

Keywords: Bulk metallic glass; Glass-forming ability; Crystallization; High pressure techniques

1. Introduction

1.1. Early developments of metallic glasses

Solid-state materials with the major bonding types including ionic, covalent, van der Waals, hydrogen, and metallic can be made by various ways into amorphous solid forms. Metallic amorphous alloys (that is, metallic glasses) are comparatively newcomers to the amorphous materials group. The formation of the first metallic glass of $Au_{75}Si_{25}$ was reported by Duwez at Caltech, USA, in 1960 [1]. They developed the rapid quenching techniques for chilling metallic liquids at very high rates of 10^5–10^6 K/s. Their work showed that the process of nucleation and growth of crystalline phase could be kinetically bypassed in some alloy melts to yield a frozen liquid configuration, that is, metallic glass. The significance of Duwez's work was that their method permits large quantities of an alloy to be made into glassy state comparing to other methods, for

* Corresponding author. Tel.: +852-2788-7831; fax: +852-2788-7830.
E-mail address: apchshek@cityu.edu.hk (C.H. Shek).

0927-796X/$ – see front matter
doi:10.1016/j.mser.2004.03.001

instance, vapor condensation. Formation, structure and property investigations of metallic glasses have attracted increasing attention because of their fundamental scientific importance and engineering application potential [2–5]. The techniques of melt quenching have been extensively developed and elaborated for the purpose of producing a wide variety of metallic glasses.

The research on metallic glasses gained more momentum in the early 1970s and 1980s when the continuous casting processes for commercial manufacture of metallic glasses ribbons, lines, and sheets [5] was developed. An explosion of academic and industrial research has resulted in that period. However, the high cooling rate limited the amorphous alloys geometry to thin sheets and lines, which are unlikely to find wide applications.

Academically, the work of Turnbull and coworker had made crucial contribution to the discipline. They illustrated the similarities between metallic glasses and other non-metallic glasses such as silicates, ceramic glasses, and polymers. It was shown in their work that, a glass transition manifested in conventional glass-forming melts could also be observed in rapid quenched metallic glasses [6,7]. The glass transition was found to occur at a rather well-defined temperature which varied only slightly as the heating rate was changed [8]. Turnbull predicted that a ratio, referred to as the reduced glass transition temperature $T_{rg} = T_g/T_m$, of the glass transition temperature T_g to the melting point, or liquidus temperature T_m of alloy, can be used as a criterion for determining the glass-forming ability (GFA) of an alloy [9]. According to Turnbull's criterion [10], a liquid with $T_g/T_m = 2/3$ becomes very sluggish in crystallization within laboratory time scale and can only crystallize within a very narrow temperature range. Such liquid can thus be easily undercooled at a low cooling rate into the glassy state. Up to now, the Turnbull criterion for the suppression of crystallization in undercooled melts remains one of the best ''rule of thumb'' for predicting the GFA of any liquid [11]. It has played a key role in the development of various metallic glasses including bulk metallic glasses (BMGs).

1.2. The birth of bulk metallic glasses

If one arbitrarily defines the millimeter scale as ''bulk'', the first bulk metallic glass was the ternary Pd–Cu–Si alloy prepared by Chen in 1974 [12]. They used simple suction-casting methods to form millimeter-diameter rods of Pd–Cu–Si metallic glass at a significantly lower cooling rate of 10^3 K/s [12]. In 1982, Turnbull and coworkers [13,14] successfully prepared the well-known Pd–Ni–P BMG by using boron oxide fluxing method to purify the melt and to eliminate heterogeneous nucleation. The fluxing experiments showed that the value of T_{rg} of the alloy could reach 2/3 when the heterogeneous nucleation was suppressed, and the bulk glass ingot of centimeter size solidified at cooling rates in the 10 K/s region. Although the formation of Pd-based BMG is an exciting achievement, owing to the high cost of Pd metal, the interests were only localized in academic field and the novelty faded after some years. Yet the activity of development of new BMG systems and related research persists.

In the 1980s, a variety of solid-state amorphization techniques, which are based on completely different mechanism from rapid quenching, such as mechanical alloying, diffusion induced amorphization in multilayers, ion beam mixing, hydrogen absorption, and inverse melting, had been developed [3]. A variety of metallic glasses in the form of thin films, or powders can be obtained by interdiffusion and interfacial reaction at temperatures well below the glass transition temperatures.

In the late 1980s, Inoue et al. in Tohoku University of Japan succeeded in finding new multicomponent alloy systems consisting mainly of common metallic elements with lower critical cooling rates [15,16]. Having systematically investigated the GFA of ternary alloys of rare-earth

materials with Al and ferrous metals, they observed exceptional GFA in the rare-earth-based alloys, for example, La–Al–Ni and La–Al–Cu [15]. By casting the alloy melt in water-cooling Cu molds, they obtained fully glassy rods and bars with thicknesses of several millimeters. Based on this work, the researchers developed similar quaternary and quinary amorphous alloys (e.g. La–Al–Cu–Ni and La–Al–Cu–Ni–Co BMGs) at cooling rates under 100 K/s and the critical casting thicknesses could reach several centimeters [17]. Some similar alloys with rare-earth metals partially replaced by the alkali-earth metal Mg, such as Mg–Y–Cu, Mg–Y–Ni, etc., were also developed [18], along with a family of multicomponent Zr-based BMGs (e.g. Zr–Cu–Ni, Zr–Cu–Ni–Al BMGs) [19].

1.3. Thermal stability and glass-forming ability of bulk metallic glasses

The formation of multicomponent BMGs demonstrated that excellent GFA is ubiquitous and not confined to Pd-based alloys. The work of Inoue opened the door to the design of new families of BMGs [16] and attention was once again focussed on the investigation on BMG [11,16]. Many kinds of BMGs have been developed including MgCuY, LaAlNi, ZrAlNiCu, ZrAlNiCu(Ti, Nb), ZrTiCuNiBe, TiNiCuSn, CuZrTiNi, NdFeCoAl, LaAlNi, FeCoNiZrNbB, FeAlGaPCB, PrCuNiAl, PdNiCuP, etc. At present, the lowest critical cooling rate for BMG formation is as low as 0.10 K/s for the $Pd_{40}Cu_{30}Ni_{10}P_{20}$ alloy and the maximum sample thickness reaches values as large as about 10 cm [21]. The alloy with the largest supercooled liquid region of 135 K is $(Zr_{82.5}Ti_{17.5})_{55}(Ni_{54}Cu_{46})_{18.75}Be_{26.25}$ [11]. The design of the ZrTiCuNiBe glass-forming alloy family was an important progress made by Peker and Johnson [20]. The quinary glass-former has distinct glass transition, very high stability of supercooled liquid state, and exhibits high thermal stability against crystallization [11]. Vitalloy 1 (vit1), one of the most extensively studied BMG in the family, has the composition of $Zr_{41}Ti_{14}Cu_{12.5}Ni_{10}Be_{22.5}$. Its temperature–time transition (TTT) diagram has the ''nose'' of the nucleation curve for crystals at time scales of the order 10^2 s and the critical cooling rates for glass formation in the 1 K/s range. The alloy can be cast in Cu-mold in the form of fully glassy rods with diameters ranging up to 5–10 cm. Fig. 1 exhibits the as-cast Zr-based BMGs in different shapes prepared by the Institute of Physics, Chinese Academy of Sciences, China. The

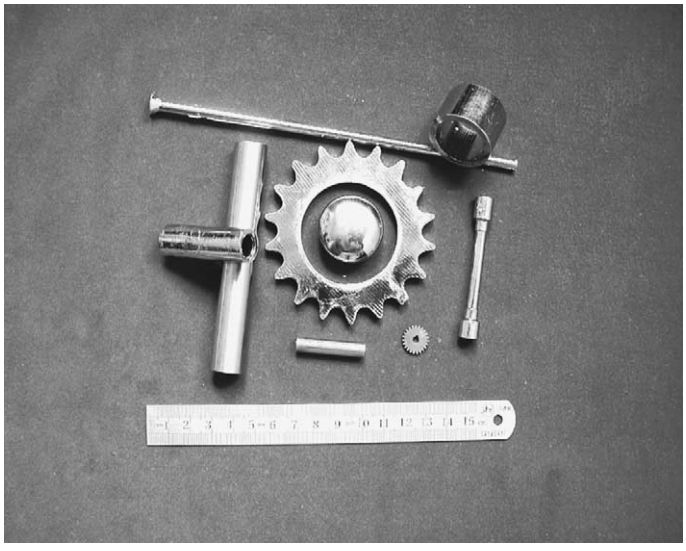

Fig. 1. The picture of as-cast vitalloy BMG system.

formation of the BMGs in this family requires no fluxing or special processing treatments and can form bulk glass by conventional metallurgical casting methods. Its GFA and processability are comparable with those of many silicate glasses. This finding makes it possible to process metallic glasses by common methods in a foundry [11]. The BMGs, which exhibit high thermal stability and superb properties, have considerable potential as advanced engineering materials. In fact, the Zr-based BMGs found applications in the industries only 3 years after its invention.

Table 1 lists the typical BMG systems and the year in which they were first reported. It is apparent that the BMGs were developed in the sequence beginning with the expensive metallic-based Pd, Pt and Au, followed by less expensive Zr-, Ti-, Ni- and Ln-based BMGs. Furthermore, it can be seen that the much cheaper Fe- and Cu-based BMGs were the most recently developed and had attracted extensive interests. Recently, the investigation on nonmagnetic bulk amorphous steel based on iron became one of the hottest topics in this field. A coordinated program has been carried out in the USA to develop new bulk ferrous metallic glasses via the exploration of novel compositions, synthesis of bulk materials, scientific underpinning of glass formability using atomistic modeling, and determination of three-dimensional atomistic structures. The new bulk iron-based metallic glasses or amorphous steel must exhibit non-ferromagnetic properties, contain minimal or zero chromium content, outperform current Naval steels in mechanical properties, and have corrosion resistance comparable to current Naval steels [35]. Fig. 2 shows a comparison of GFA of various glasses. One can clearly see that some excellent bulk glass former has a GFA very close to silicate glasses. Table 2 lists the typical BMGs with thermal parameters and GFA represented by T_{rg}.

Table 1
Bulk metallic glasses and their developed year

BMG system	Years	Reference
Pd–Cu–Si	1974	[12]
Pt–Ni–P	1975	[29]
Au–Si–Ge	1975	[29]
Pd–Ni–P	1982	[13]
Mg–Ln–Cu (Ln = lanthanide metal)	1988	[15]
Ln–Al–TM (TM = group transition metal)	1989	[17]
Zr–Ti–Al–TM	1990	[18]
Ti–Zr–TM	1993	[16]
Zr–Ti–Cu–Ni–Be	1993	[20]
Nd(Pr)–Al–Fe–Co	1994	[30]
Zr–(Nb, Pd)–Al–TM	1995	[11]
Cu–Zr–Ni–Ti	1995	[31]
Fe–(Nb, Mo)–(Al, Ga)–(P, C, B, Si, Ge)	1995	[16]
Pd–Cu(Fe)–Ni–P	1996	[21]
Co–(Al, Ga)–(P, B, Si)	1996	[16]
Fe–(Zr, Hf, Nb)–B	1996	[16]
Co–Fe–(Zr, Hf, Nb)–B	1996	[16]
Ni–(Zr, Hf, Nb)–(Cr, Mo)–B	1996	[16]
Ti–Ni–Cu–Sn	1998	[16]
LaAlNiCuCo	1998	[32]
Ni–Nb	1999	[33]
Ni–(Nb, Cr, Mo)–(P, B)	1999	[16]
Zr-based glassy composites	1999	[25]
Zr–Nb–Cu–Fe–Be	2000	[34]
Fe–Mn–Mo–Cr–C–B	2002	[35]
Ni–Nb–(Sn, Ti)	2003	[36]
Pr(Nd)–(Cu, Ni)–Al	2003	[37]

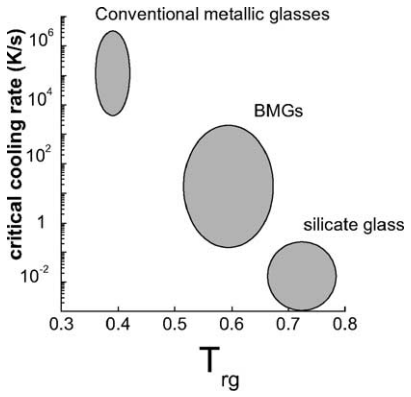

Fig. 2. A comparison of critical cooling rate and reduced glass transition temperature T_{rg} for BMG, silicate glasses and conventional metallic glasses.

Over the past decade, various methods have been developed to produce metallic glasses in bulk. One of the general guiding principles to designing alloys that form BMGs is to pick elements with large differences in size, which leads to a complex structure that crystallizes less easily. The addition of beryllium, which is much smaller in size than zirconium atom, into Zr-based alloy increases the GFA significantly [11]. Another effective step is to look for alloy compositions with deep eutectics, which form liquids that are stable to relatively low temperatures [11]. Addition methods are also widely used to find the new bulk glass-forming alloys [23]. For example, a proper addition of Cu in PdNiP alloy, Be in Zr-based alloy, Sn on the Ti- and Cu-based alloy, lithium addition and silver addition in the MgCuY alloy greatly improve the GFA of the respective alloys and get new BMG systems [11,16]. For the preparation of Fe-based glass-forming alloys, $Fe_{80}B_{20}$ is often used as the starting alloy; by adding some metals with high melting temperature, such as Zr, Nb, Ta, W and Mo, Fe-based BMGs with 5 mm diameters can be obtained by copper mould casting [16,22]. Addition method was also found to improve effectively the properties and processability of the BMGs [23,24].

The bulk metallic glass formers are very robust against some heterogeneous nucleation sites at the surface or at interfaces. This leads to the development of bulk metallic glassy matrix composites by the addition of special crystalline materials [25–27]. For example, a small change of Nb composition results in a substantially improved GFA and ductility of the bulky glass-forming system [27]. Dissolution of minute amount of metalloid elements into the Zr–Ti–Cu–Ni–Be metallic glass system can enlarge the thermal stability and hardness of the BMG [28]. Introducing ceramics such as carbon fibers, SiC, carbon nanotube, WC and ZrC particles directly into BMGs also yields BMG-based composites with excellent properties [11]. Therefore, synthesis of metallic glassy matrix composite with improved mechanical and other properties is a promising way for broadening the applications of the BMGs.

Ever since the discovery of metallic glasses by Duwez and coworkers, much research effort has been devoted to the study of the thermodynamics and thermophysical properties like viscosity, relaxation, diffusion, etc. of metallic glass. Nevertheless, the lack of thermal stability in the supercooled liquid state of metallic systems with respect to crystallization did not allow such studies in the supercooled liquid region. Most studies were done below or in the vicinity of the glass transition region. The novel BMG-forming liquids can now be studied in a much broader time and temperature ranges. They provide large experimental temperature and time windows for measuring their physical properties, as well as for studying nucleation and growth in supercooled liquid state and glass transition. It is now even possible to measure their time–temperature transformation (TTT)

Table 2
The composition of representative BMG systems, their glass transition temperature, T_g, onset temperature of crystallization, T_x, and onset melting point, T_m, and glass-forming ability represented by reduced glass transition temperature, T_{rg}

BMG	T_g (K)	T_x (K)	T_m (K)	T_{rg}
$Mg_{80}Ni_{10}Nd_{10}$	454.2	477.7	725.8	0.63
$Mg_{65}Ni_{20}Nd_{15}$	459.3	501.4	743.0	0.62
$Mg_{75}Ni_{15}Nd_{10}$	450.0	482.8	717.0	0.63
$Mg_{70}Ni_{15}Nd_{15}$	467.1	494.1	742.5	0.63
$Mg_{65}Cu_{25}Y_{10}$	424.5	484.0	727.9	0.58
$Zr_{41.2}Ti1_{3.8}Cu_{12.5}Ni_{10}Be_{22.5}$	623.0	705.0	932.0	0.67
$Zr_{46.25}Ti_{8.25}Cu_{7.5}Ni_{10}Be_{27.5}$	622.0	727.0	909.0	0.68
$Zr_{45.38}Ti_{9.62}Cu_{8.75}Ni_{10}Be_{26.25}$	623.0	740.0	911.0	0.68
$Zr_{42.63}Ti_{12.37}Cu_{11.25}Ni_{10}Be_{23.75}$	623.0	712.0	933.0	0.67
$Zr_{44}Ti_{11}Cu_{10}Ni_{10}Be_{25}$	625.0	739.0	917.0	0.68
$Zr_{38.5}Ti_{16.5}Ni_{9.75}Cu_{15.25}Be_{20}$	630.0	678.0	921.0	0.68
$Zr_{48}Nb_8Cu_{12}Fe_8Be_{24}$	658	751	1009	0.65
$Zr_{48}Nb_8Cu_{14}Ni_{12}Be_{18}$	656	724	997	0.66
$Zr_{57}Ti_5Al_{10}Cu_{20}Ni_8$	676.7	725.4	1095.3	0.62
$Zr_{57}Nb_5Cu_{15.4}Ni_{12.6}Al_{10}$	687	751	1092	0.63
$Zr_{53}Ti_5Cu_{16}Ni_{10}Al_{16}$	697	793	1118	0.62
$Zr_{66}Al_8Cu_7Ni_{19}$	662.3	720.7	1117.3	0.59
$Zr_{66}Al_8Cu_{12}Ni_{14}$	655.1	732.5	1109.1	0.59
$Zr_{66}Al_9Cu_{16}Ni_9$	657.2	736.7	1110.9	0.59
$Zr_{66}Al_8Ni_{26}$	672.0	707.6	1188.5	0.57
$Zr_{65}Al_{7.5}Cu_{17.5}Ni_{10}$	656.5	735.6	1108.6	0.59
$Pd_{40}Ni_{40}P_{20}$	590.0	671.0	877.3	0.67
$Pd_{81.5}Cu_2Si_{16.5}$	633.0	670.0	1008.8	0.63
$Pd_{40}Cu_{30}Ni_{10}P_{20}$	586.0	678.0	744.8	0.79
$Pd_{42.5}Cu_{30}Ni_{7.5}P_{20}$	574.0	660.0	808.0	0.71
$Pd_{77.5}Cu_6Si_{16.5}$	637.0	678.0	1019.4	0.62
$Pd_{42.5}Cu_{27.5}Ni_{10}P_{20}$	572.0	666.0	752.0	0.76
$Cu_{60}Zr_{30}Ti_{10}$	713.0	763.0	1110.0	0.64
$Cu_{54}Zr_{27}Ti_9Be_{10}$	720.0	762.0	1090.0	0.66
$Cu_{60}Zr_{20}Hf_{10}Ti_{10}$	754	797	1189	0.63
La66Al14Cu20	395.0	449.0	681.9	0.58
$La_{55}Al_{25}Ni_{20}$	490.8	555.1	711.6	0.69
$La_{55}Al_{25}Ni_{10}Cu_{10}$	467.4	547.2	662.1	0.71
$La_{55}Al_{25}Cu_{20}$	455.9	494.8	672.1	0.68
$La_{55}Al_{25}Ni_5Cu_{10}Co_5$	465.2	541.8	660.9	0.70
$Nd_{60}Al_{10}Cu_{10}Fe_{20}$	485.0	610.0	773.0	0.63
$Nd_{60}Al_{15}Ni_{10}Cu_{10}Fe_5$	430.0	475.0	709.0	0.61
$Nd_{61}Al_{11}Ni_8Co_5Cu_{15}$	445.0	469.0	729.0	0.61
$Ti_{34}Zr_{11}Cu_{47}Ni_8$	698.4	727.2	1119.0	0.62
$Ti_{50}Ni_{24}Cu_{20}B_1Si_2Sn_3$	726.0	800.0	1230.0	0.59
$Au_{77.8}Si_{8.4}Ge_{13.8}$	293.0	293.0	606.0	0.48
$Pr_{60}Cu_{20}Ni_{10}Al_{10}$	409	452	705	0.58
$Pr_{55}Al_{12}Fe_{30}Cu_3$	551	626	845	0.65

Most of data were obtained by DSC or/and DTA at a heating rate of 20 K/min.

diagrams, such as the one shown in Fig. 3 for $Zr_{41.2}Ti_{13.8}Cu_{10.0}Ni_{12.5}Be_{22.5}$ alloy. In Fig. 3, the onset times for isothermal crystallization are plotted as a function of temperature. The data were obtained by electrostatic levitation and crystallization in high-purity graphite crucibles. The diagram shows the typical ''C'' curve and a minimum crystallization time of 60 s at 895 K. For previously known glass-forming alloys, the times were of the order of milliseconds, implying the need for rapid quenching for vitrification. The TTT diagram of vit1 reflects a very low critical cooling rate of about 1 K/s, which is five orders of magnitude lower than those in earlier metallic glass-forming systems.

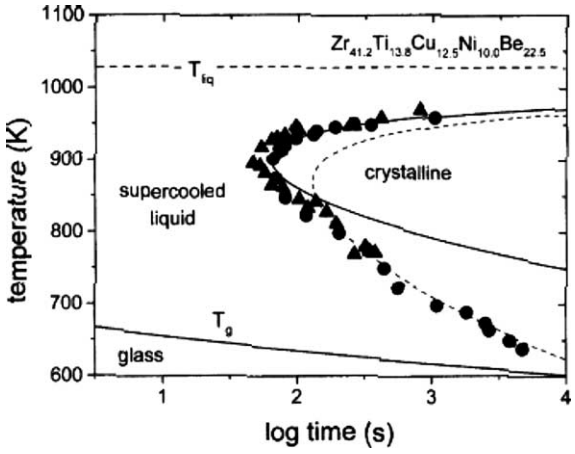

Fig. 3. A time–temperature-transformation diagram for the primary crystallization of V1. Data obtained by electrostatic levitation (●) and processing in high-purity carbon crucibles (▲) are included [45]. (Copyrighted by The Minerals, Metals and Materials Society (TMS).)

The ''C'' shape is the result of the competition between the increasing driving force for crystallization and the slowing down of kinetics (effective diffusivity) of atom movement. With extensive experimental data on the formation of the BMG available, empirical rules for the achievement of large GFA were proposed [11,16]. Nevertheless, the formation mechanism of the multicomponent BMGs and the main factors which influence the GFA have not been clearly elucidated. Over time, the discovery of new and better glass formers has prompted a search for a comprehensive underlying rule for predicting the GFA based on thermodynamic, kinetic and structural properties of alloys. The development of multicomponent alloys with exceptional glass-forming ability will continue. The progress depends, to a large extend, on the in-depth understanding of the formation mechanism and improvement of the preparation techniques.

2. Glass formation and crystallization in bulk metallic glass-forming alloys

2.1. Understanding of glass formation from thermodynamic, kinetic and microstructure aspects

Early approaches to fabrication of BMG were mostly empirical in nature, but researchers gradually began to understand that the correct choices of elemental constituents would lead to amorphous alloys exhibiting critical cooling rates as slow as 1–100 K/s. These slower cooling rates mean that large pieces of metallic glasses can be fabricated. For the new types of metallic glass-forming alloys the intrinsic factors of the alloys (such as the number, purities and the atomic size of the constituent elements, composition, cohesion among the metals, etc.) instead of external factors (such as cooling rate, etc.) play key roles in the glass formation. In general, the GFA in BMGs tends to increase as more components are added to the alloy. That is called the ''confusion principle'' [38], which implies that larger number of components in an alloy system destabilizes competing crystalline phases which may form during cooling. This effect frustrates the tendency of the alloy to crystallize by making the melt more stable relative to the crystalline phases. Inoue summarized the results of glass formation in multicomponent alloys and proposed three empirical rules [16]: (1) multicomponent systems consisting of more than three elements; (2) significant difference in atomic sizes with the size ratios above about 12% among the three main constituent elements; and

(3) negative heats of mixing among the three main constituent elements. They claimed that the alloys satisfying the three empirical rules have special atomic configurations in the liquid state which are significantly different from those of the corresponding crystalline phases. The atomic configurations favor the glass formation in terms of thermodynamics, kinetics as well as the microstructure development.

The ability to form a glass by cooling from an equilibrium liquid is equivalent to suppressing crystallization within the supercooled liquid. If the steady-state nucleation is assumed, the nucleation rate is determined by the product of a thermodynamic and a kinetic factor as shown:

$$I = AD \exp\left[-\frac{\Delta G^*}{kT}\right] \tag{2.1}$$

where A is a constant, k the Boltzmann's constant, T the absolute temperature, D the effective diffusivity and ΔG^* the activation energy which must be overcome for the formation of stable nuclei. From classical nucleation theory, ΔG^* can be expressed as $\Delta G^* = 16\pi\sigma^3/3(\Delta G_{\mathrm{l-s}})^2$, where σ is the interfacial energy between the nuclei and liquid phase, and $\Delta G_{\mathrm{l-s}} = G_{\mathrm{l}} - G_{\mathrm{s}}$ is the free-energy difference between the liquid state G_{l} and crystalline state G_{s}. $\Delta G_{\mathrm{l-s}}$ is therefore the driving force for crystallization. Based on the above considerations, the driving force (thermodynamic factor), diffusivity or viscosity (kinetic factor) and configuration (structural factor) are crucial parameters for understanding the glass formation in multicomponent alloys. These factors will be discussed in the following sections.

2.1.1. Thermodynamic aspects

From thermodynamics considerations, bulk glass formers naturally exhibit a low driving force for crystallization in the supercooled liquid. The low driving force results in low nucleation rates and therefore improved GFA. Thermal analysis allows the determination of the Gibbs free-energy difference $\Delta G_{\mathrm{l-s}}$ between the supercooled liquid and crystalline solid. Generally, it has been found that high GFA is favored by small values of $\Delta G_{\mathrm{l-s}}$, which can be calculated by integrating the specific heat capacity difference $\Delta C_{\mathrm{p}}^{\mathrm{l-s}}(T)$ according to the equation

$$\Delta G_{\mathrm{l-s}}(T) = \Delta H_{\mathrm{f}} - \Delta S_{\mathrm{f}} T_0 - \int_T^{T_0} \Delta C_{\mathrm{p}}^{\mathrm{l-s}}(T)\,\mathrm{d}T + \int_T^{T_0} \frac{\Delta C_{\mathrm{p}}^{\mathrm{l-s}}(T)}{T}\,\mathrm{d}T \tag{2.2}$$

where ΔH_{f} and ΔS_{f} are the enthalpy and entropy of fusion, respectively, at the temperature T_0, the temperature at which the crystal and the liquid are in equilibrium. A low $\Delta G_{\mathrm{l-s}}$ means a small enthalpy of fusion ΔH_{f} and a large entropy of fusion ΔS_{f}. The large ΔS_{f} is expected to be associated with multicomponent alloys because ΔS_{f} is proportional to the number of microscopic states [39]. The free energy at a constant temperature also decreases in the case of low chemical potential caused by the low enthalpy and high value of T_{rg} as well as the large liquid/solid interfacial energy [39]. Therefore, the increase in the number of alloy components leads to the increase in ΔS_{f} and causes the increase in the degree of dense random packing in the liquid state. This is favorable for the decrease in ΔH_{f} and the solid/liquid interfacial energy. The concept is consistent with the "confusion principle" [38] and Inoue's first empirical rule [16].

Based on the thermodynamic data, Busch et al. [40,41] had systematically studied the thermodynamic functions of the typical bulk glass-forming undercooled liquid, and the thermodynamic functions of the undercooled liquid were calculated using a $1/T^2$ dependence of the specific heat capacity. Fig. 4 shows the specific heat capacities in the supercooled liquid for several alloys. Fig. 5 illustrates the calculated entropy of the undercooled vit1 melt with respect to

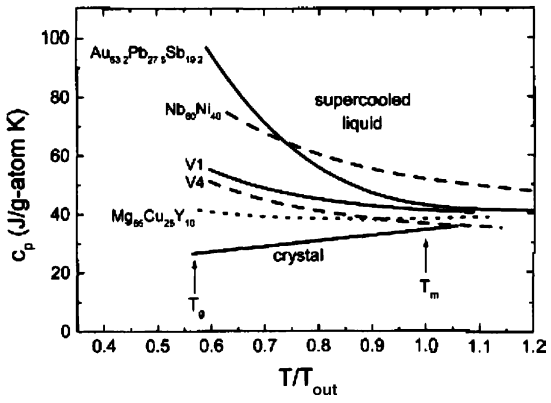

Fig. 4. Specific heat capacities in the supercooled liquid for several alloys normalized to the eutectic temperature, T_{eut} [41]. (Reproduced by the kind permission of American Institute of Physics.)

the crystal. The entropy of the undercooled liquid decreases with increasing undercooling until it reaches the entropy of the crystal at the Kauzmann temperature, T_K. The calculated Gibbs free-energy function with respect to the crystalline state is shown in Fig. 6, from which it can be seen that for larger undercoolings, the real Gibbs free-energy difference becomes smaller due to the relative stabilization of the undercooled melt. This stabilization is attributed to the increasing specific heat capacity which arises from a decreasing free volume, and probably a gradual gain of short-range order in the alloy melt as well. The observed Gibbs free-energy difference is, for example, 1.5 kJ/mol at $0.8T_m$. This value is relatively small compared to conventional binary glass-forming alloys like $Ni_{50}Ti_{50}$ or $Nb_{50}Ni_{50}$ at $0.8T_m$, where Gibbs free-energy differences of 2.5 and 3.2 kJ/mol, respectively, are found. The calculated Gibbs free-energy difference between liquid and solid state stays small even for large undercoolings. This relatively small Gibbs free-energy difference is considered to be a contributing factor in the high GFA of the alloy [40].

Fig. 7 exhibits the Gibbs free-energy difference between the supercooled liquid and the crystalline mixture for different glass-forming alloys [41]. The Gibbs free-energy difference is compared with those of other typical eutectic, or close to eutectic, glass-forming systems. The alloys show different critical cooling rates between 1 K/s for the vit1 and about 10^4 K/s for the binary

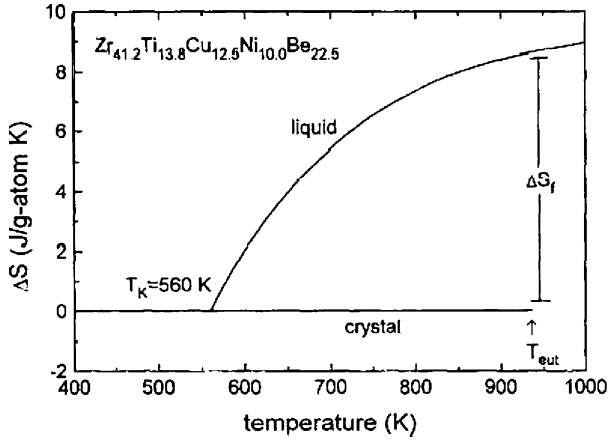

Fig. 5. The calculated entropy of the undercooled $Zr_{41}Ti_{14}Cu_{12.5}Ni_{10}Be_{22.5}$ melt with respect to the crystal [40]. (Reproduced by the kind permission of American Institute of Physics.)

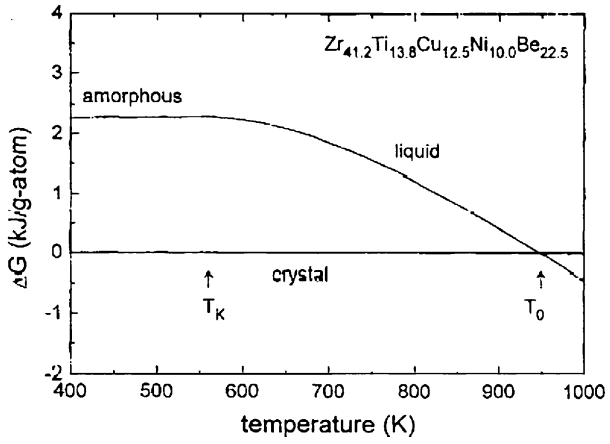

Fig. 6. The calculated Gibbs free-energy function with respect to the crystalline state [40]. (Reproduced by the kind permission of American Institute of Physics.)

$Zr_{62}Ni_{38}$. The glass formers with the lower critical cooling rates have smaller Gibbs free-energy differences with respect to the crystalline state than the glass formers with high critical cooling rates. The small free-energy difference of these deep eutectic bulk metallic glass-forming systems in the melt suggests that they already have a small free volume and a tendency to develop chemical short-range order at or close to the melting point. These findings are consistent with the assumption that in multicomponent systems the crystalline phases exhibit relatively large configurational entropies of mixing and with the fact that bulk metallic glass formers are very viscous and relatively dense liquids at the melting point and upon undercooling [41].

The multicomponent alloys with excellent GFA have low melting temperature as shown in Table 2. In view of this, high GFA alloys can be found among alloy compositions with deep eutectics, which form liquids that are stable to relatively low temperatures. Therefore, $T_{rg} = T_g/T_m$ is a key parameter for glass formation, and the homogeneous nucleation rate in the undercooled melt is a strong function of the parameter. Searching through binary phase diagrams, one find that the best candidates for good glass formers are systems such as Pd–Si, Pd–P, Ni–Nb, Cu–Zr and Zr–Be, which all exhibit deep eutectics. In the ternary ZrTiCu, one find the composition at the even deeper eutectic

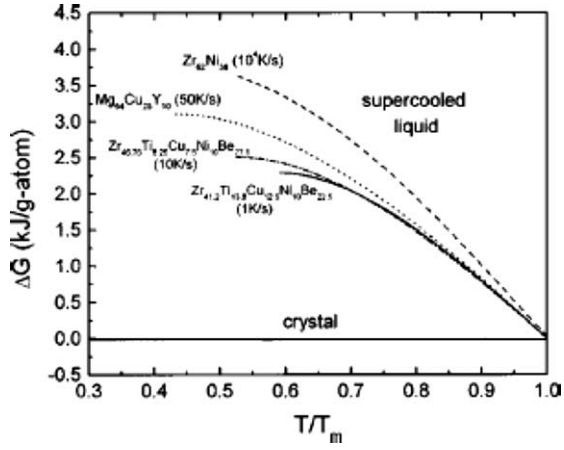

Fig. 7. Gibbs free-energy difference between the supercooled liquid and the crystalline mixture for different glass-forming alloys [41]. (Reproduced by the kind permission of American Institute of Physics.)

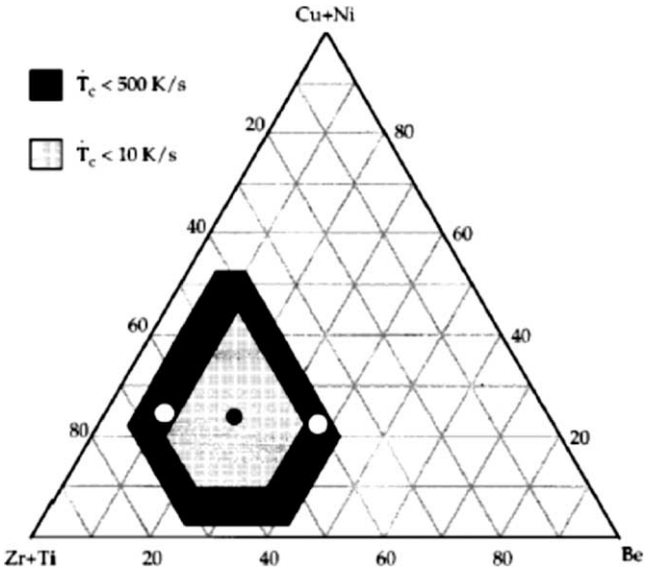

Fig. 8. Quasi-ternary cut through the Zr–Ti–Cu–Ni–Be phase diagram. The compositions of the initial $Zr_{41.2}Ti_{13.8}Cu_{12.5}Ni_{10.0}Be_{22.5}$ melt (●) is marked [43]. (Reproduced by the kind permission of American Institute of Physics.)

has better GFA [42]. The situation is further improved by taking quaternary alloys of Cu–Ti–Ni–Zr [31,11]. Near the quaternary eutectic compositions, the good glass former of $Ti_{34}Zr_{11}Ni_8Cu_{48}$ alloy with $T_{rg} = 0.6$ and critical cooling rate of 50–100 K/s was obtained [31]. For higher-order ZrTiCuNiBe alloy, a deeper eutectic features in the slightly off-center portion of the quinary phase diagram shown in Fig. 8 [43]. The thermodynamic competitiveness of the crystalline phases is diminished relative to the more accommodating liquid phase, resulting in a very deep higher-order ''eutectic'' structure with high GFA. In the central shaded part of Fig. 8, the liquidus temperature T_l is as low as 973 K, and the values of T_{rg} are ranging from 0.65 to 0.7. According to Turnbull's criterion, one can predict that the nucleation will be very difficult in the alloys. Apart from T_{rg}, another extensively used parameter for GFA is ΔT_x $(= T_x - T_g)$, which is equal to the difference between the onset temperature of the first crystallization peak (T_x) and the glass transition temperature. However, the comparison of GFA based on T_{rg} and ΔT_x do show significant discrepancies in some alloy systems. A refined parameter taking T_x, T_g and T_l into account was therefore proposed recently by Lu and Liu [44]. They found that the parameter $\gamma = T_x/(T_g + T_l)$ gave better reference for judging the GFA among metallic glasses.

2.1.2. *Kinetics aspects*

Glass transition from melt state to glassy state cannot be described as a thermodynamic phase transition despite the discontinuity in the specific heat observed at glass transition. The glass transition temperature depends on the experimental cooling or heating rate during measurements. To better characterize the GFA of BMG systems, one needs to study the crystallization kinetics in these alloys. From the perspective of kinetics, the parameters such as viscosity have a significant influence on the GFA of an alloy system. A variety of techniques have been applied to measure viscosity from the equilibrium liquid down to the deeply undercooled liquid near T_g [43,45,46]. Since the undercooled liquid alloys are relatively stable with respect to crystallization on laboratory time scales, viscosity can be measured in bulk glass-forming systems in much wider temperature and time scales than before. Fig. 9 shows the viscosities of the BMG known as vit4 measured with parallel

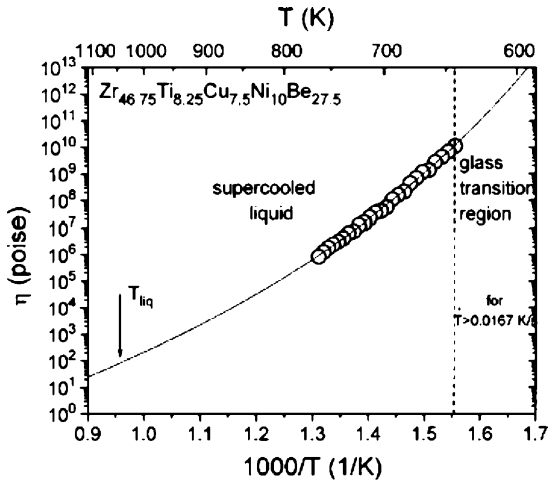

Fig. 9. Viscosity as a function of temperature for the undercooled liquid of vit4. The precision of the measurement is better than the size of the symbols. Also shown is the Vogel–Fulcher fit to the data [48]. (Reproduced by the kind permission of American Institute of Physics.)

plate rheometry methods [47,48]. It can be seen from Fig. 9 that the data cover 15 orders of magnitude, and all viscosity data η can be described well with the Vogel–Fulcher–Tammann (VFT) relation [49]:

$$\eta = \eta_0 \exp\left[\frac{DT_0}{T - T_0}\right] \tag{2.3}$$

where T_0 is the Vogel–Fulcher temperature, at which the barriers with respect to flow would go to infinity. D is known as the fragility parameter which identifies the property of liquid [49]. It is found that the apparent singularity at T_0 for vit4 in the VFT equation occurs far below the calorimetric glass transition. This is in contrast to what was generally expected from early work on metallic alloys. This indicates that the BMG-forming liquid behave kinetically much closer to silicate melts which have excellent GFA.

The change of viscosity of a liquid as a function of undercooling can be used to characterize and classify the different liquids [49], because it reflects the change of mobility of atom during supercooling. Fig. 10 compares the viscosities of some typical BMGs with a selection of typical non-metallic liquids [11]. SiO_2 is the strongest glass former with the fragility D of about 100. It exhibits a very small VFT temperature and a very high melt viscosity. On the other hand, *O*-terphenyl is the typical fragile glass with a fragility of 5 [50] and low melt viscosity. It shows a more abrupt change in the kinetics close to the glass transition. The available viscosity data of BMG forming liquids show that they behave closer to strong glasses than fragile glasses and have fragility (D) approximately equal to 20. The melt viscosity of BMGs is in the order of 2–5 Pa s and is about three orders of magnitude more viscous than pure metals, which usually have viscosities of the order of 10^{-3} Pa s [11]. The relaxation behavior of the BMG forming liquids studied by neutron scattering is also similar to the nature of strong liquids [51,52]. The strong liquid behavior implies high viscosity and sluggish kinetics in the supercooled liquid state. This greatly retards the formation of stable nuclei in the melt. The growth of the thermodynamically favored phases is inhibited by the poor mobility of the constituents. The nucleation and growth of the crystalline phase in supercooled liquid state is very difficult and thus lead to large GFA and high thermal stability of the supercooled liquid state. Fig. 11 illustrates the schematic diagram showing the high stability of the BMG forming

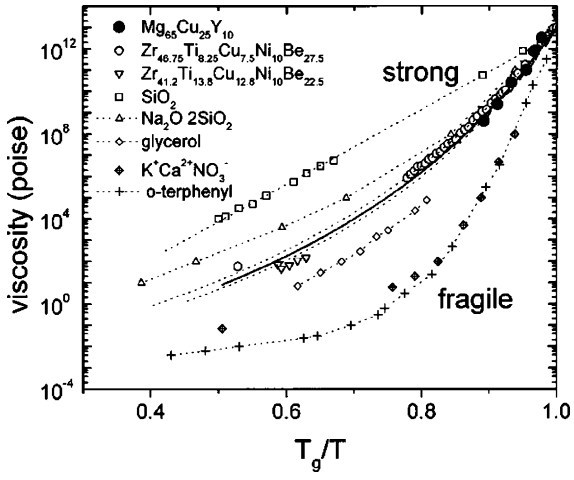

Fig. 10. A comparison of viscosity of various glass-forming liquids. The plot shows that the BMG forming liquid can be classified into strong liquid [41]. (Reproduced by the kind permission of American Institute of Physics.)

supercooled liquid for up to several thousands of second. The conventional metallic glasses have nucleation kinetics in undercooled region such that the onset time for crystallization was in the regime of 10^{-4} to 10^{-3} s at the ''nose'' of the C-curve. For BMG forming systems, there can be C-curves with noses at time scale of the order of 100–1000 s.

The mechanisms of atomic transport in supercooled liquids are long-standing problems. Collective atomic motion is thought to play an important role in supercooled liquids. A BMG forming supercooled liquid represents an ideal system for studying intrinsic collective motions because of its stability and structural similarity to the ''dense random packing of spheres'' model, which is conceptually simple. The results of Geyer et al. [53] on Be diffusion in glassy state and supercooled liquid, respectively, of vit1 are shown in Fig. 12. It was found that the apparent activation energy for diffusion in glass is much smaller than that of the supercooled liquid. They attributed this to a crossover in behavior from Be hopping in an essentially solid environment to Be transport by cooperative shearing in the liquid state. Tang et al. [54,55] reported a ^{9}Be nuclear

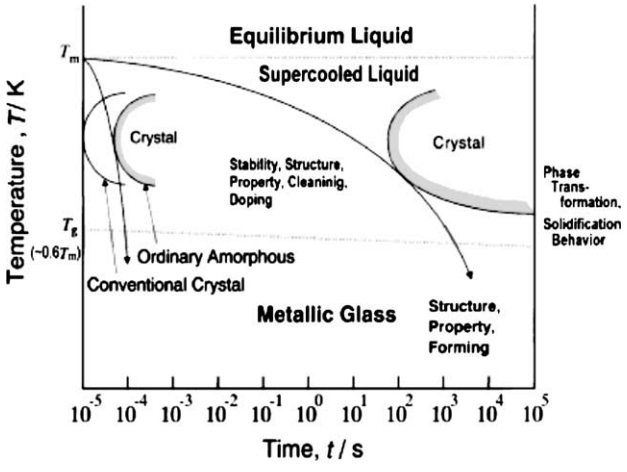

Fig. 11. The schematic diagram showing the high stability of the BMG forming supercooled liquid for long periods reaching several thousands of second [77]. (Copyright (2002) by The Japan Institute of Metals.)

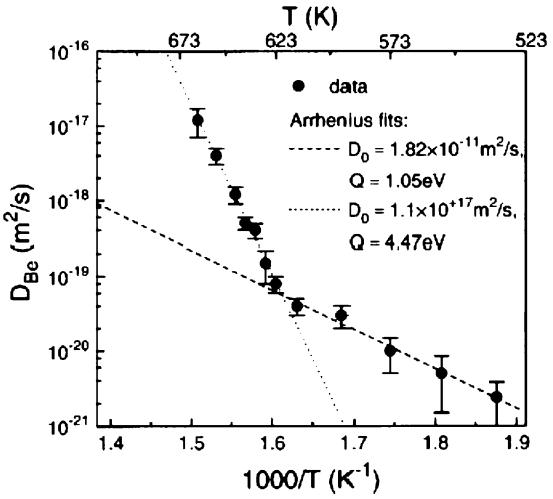

Fig. 12. Arrhenius plot of the self-diffusivity of Be in $Zr_{41.2}Ti_{13.8}Ni_{10}Cu_{12.5}Be_{22.5}$ (solid circles) and two Arrhenius fits to the data (lines) [53]. (Copyright (1995) by the American Physical Society.)

magnetic resonance study of Zr-based bulk metallic glasses and the microscopic transport in supercooled liquids around the glass transition regime was investigated. Combining with diffusion measurements, they demonstrated that two distinct processes, namely, single-atom hopping and collective motion, contributed to long-range transport in the supercooled liquid state, with the latter being the dominant process. The effect of the glass transition is clearly visible in the observed diffusion behavior of the Be atoms as shown in Fig. 13. The phenomena demonstrated a new paradigm for understanding atomic diffusion in liquid metals. Much more work could be done in this field.

2.1.3. Electronic effects on structural stability

The aforementioned stabilizing factors relevant to atomic structures, a priori, originates from the electronic structure of a metallic glass. The microscopic theory concerning the relationship

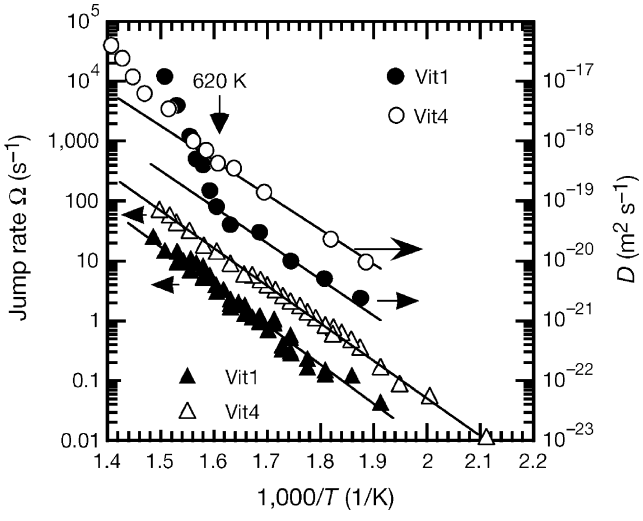

Fig. 13. The temperature dependence of the interdiffusion coefficients of Be in vit1 and vit4 [55]. (Reproduced with the kind permission of Nature Publishing Group.)

between the atomic and the electronic structures present more fundamental understandings on the structural stability of a solid phase, regardless of the crystalline or disordered nature. Nagel and Tauc [56] treated a metallic glass as a nearly free electron metal and the dominant influence of conduction electrons on the structure factors has been used to understand the stability of a metallic glass against crystallization. They proposed that a metallic glass is stabilized when the Fermi level E_F is located at a minimum in the density-of-state curve. This would occur when the Fermi surface and the diffused pseudo-Brillouin zone boundary of the glassy phase coincide. In such a case, the basic characteristic wave numbers, $2k_f$ and k_p, are equal, where $2k_f$ is the diameter of the Fermi sphere and k_p is the first peak of the static structure factor. As a sequence, they argued that the effect of alloying would cause the rigid shift of $2k_f$ with respect to k_p. As $2k_f$ moves away from k_p, the system would become less stable against crystallization and thereby have a lower T_g [57,58].

Beck and Oberle [59] discussed the pair distribution function $g(r)$ and the pair potential $\phi(r)$ of metallic glasses and pointed out that the stability is obtained if the consecutive maxima of $g(r)$ coincide with the minima of $\phi(r)$. This eventually also leads to the condition, $2k_f = k_p$. The criterion implies that the pseudogap in the density-of-state curve is a necessary condition. Under this situation, the falling of the Feimi level on the declining slope of the pseudogap naturally contributes to lowering the total kinetic energy of electrons thereby reducing the system energy.

Häussler et al. [60] deduced from the measured ultraviolet photoelectron spectra the presence of a structure-induced density-of-state pseudogap in the vapor-deposited amorphous Cu–Sn and Au–Sn thin films. This is also the universal feature of most of the noble metal-simple polyvalent metal alloys, and the glass-forming composition with the concentration of conduction electrons (*e/a*, electron concentration per atom) of 1.8 is proposed as the 'ideal amorphous state' [61]. For the electronically simple metallic glasses, $2k_f$ is well defined. Mizutani [62] constructed a two-dimensional map in terms of $2k_f/k_p$ and the size ratio r/R, and they summarized that glass formation, as obtained by liquid quenching, occurs at an extended $2k_f/k_p$ span between 0.8 and 1.2 when r/R is in the range 0.5–0.8.

However, for alloys containing transition metals (TMs), the total density-of-states deviate significantly from the near-free-electron parabola due to the existence of the d-states in their valence bands, the rather small effect induced by structure would be masked if the Fermi level falls in the d-band. Experimentally, pseudogaps were not observed in the Cu–Zr [62] and Pd–Si [63] metallic glasses, and not even in the Cu-containing Hume-Rothery-type Au–Cu–Mg metallic glasses [64].

To predict glass formation, the criteria based on the atomic size factor provide a good tool to determine the composition range in a given system. The electronic structure viewpoints present more fundamental picture on the stability of metallic glasses. The connection between them is the bridge to the prediction of glass formation. This viewpoint has been well verified in binary systems in which the glass-forming composition ranges can be experimentally determined. The recent work of Dong and coworkers [71,73–75]. indicates that the GFAs and thermal stabilities of BMGs are closely related to the conduction electron concentration *e/a* and the atomic size factor. The empirical criteria in combination with phase diagram characteristics have been used to predict the high GFA regions in Zr-based alloys, which constitute the main topics in the following discussion.

2.1.3.1. e/a-based criterion for Zr-based BMGs—assignment of effective e/a for transition metals. The *e/a*-scaled structural stabilization and the specific *e/a* for the largest stability is a simple and promising criterion in the search of high GFAs in a given system. This is especially favorable for the multicomponent systems, as the criterion is not depending specifically on the element involved. Therefore it is well worth considering the compliance of a real alloy system with the $2k_f = k_p$ rule.

The condition that the Fermi surface makes contacts with a number of equivalent Brillouin Zone planes have been revealed both theoretically and experimentally in the transition-element-containing

Hume-Rothery phases. Generally an assignment of the effective *e/a* values of TMs is recommended to explain the phase stability by using the matching rule [65–68]. For a further clarification, Mizutani et al. [69] demonstrated that particular FS–BZ interactions are strongly coupled with the sp-d hybridization to produce a deep pseudogap across the Fermi level by using the LMTO-ASA (linear muffin-tin orbital-atomic sphere approximation) band calculations. The validity of the matching rule for systems involving d states in the valence band was well explained by distinguishing the long-range-order-related FS–BZ zone effects from the short-range-order-related sp-d hybridization effect. For the assignment of an effective *e/a* value of a transition metal component, diffraction experiments can be used. Friedel [70] pointed out that strong intensities of a few families of diffraction peaks observed by X-ray and fast electron scattering result from the interaction between X-ray (or fast electron) and the effective potential. The predominant BZs then correspond to the intense peaks in a diffraction pattern. Following this method, Dong et al. studied the crystallization products of the Zr-based multicomponent BMGs, and for a more universal discussion, we also included the (Zr, Ti)-based quasicrystals and their approximants were also included [71].

An effective *e/a* of 1.5 assigned to the solvent element Zr explained effectively the contacting situation for all these phases (Table 3). Furthermore, Dong et al. notice that the BMG-related and the quasicrystal-related phases in a given system are a family of Hume-Rothery phases sharing nearly the same *e/a* ratios [71]. For a glassy phase, the wave numbers $k_p = 4\pi \sin\theta_p/\lambda$ are obtained from the diffraction angel θ_p of the principal diffuse peak in their XRD patterns. This indicates the basic role of the *e/a* factor in stabilizing these Hume-Rothery phases containing a large number of atoms per unit cell. However, the fundamental aspects of the phenomenon are far from clarified in the present discussion. The aforementioned phenomena indicate that the formation and stabilities of the Zr-based BMGs, their quasicrystalline and crystalline counterparts are inter-related. This coincidence opens a new route in the search of the compositions with large GFAs in a given system. The known crystalline phases can be employed to establish the specific *e/a*-constant lines or planes in ternary or quaternary systems, respectively. The ''constant *e/a* rule'' in the BMG-related phases, including quasicrystals and crystalline counterparts, should be a useful composition guideline for designing alloys with large GFA.

2.1.3.2. The e/a-constant criterion in the Zr–Al–Ni system. The *e/a*-constant phenomenon can be better visualized in phase diagrams. In the Zr–Al–Ni system, three known phases, $Al_{50}Ni_{50}$ (CsCl structure), ZrAlNi (Fe_2P structure) and pure Zr, fall on the line with $e/a = 1.5$. $Zr_{60}Al_{20}Ni_{20}$, the composition reported with the largest GFA in the Zr–Al–Ni system [72], lie exactly on this e/a-constant line (Fig. 14) [71].

Phase diagrams are available for the ternary Zr–Al–X systems, where X is either Fe, Co, Ni or Cu. The 1.5 e/a-constant line is found to be a common feature in these systems. Dong et al. demonstrated recently the formation of BMGs with large GFA on this line in Zr–Al–Co [73] (Fig. 15) and Zr–Al–Ni(Co) (Fig. 16) systems [74].

2.1.3.3. The e/a-constant criterion in the Zr–Al–Ni–Cu system. The quasicrystal is often the primary devitrification product of oxygen-containing Zr-based BMGs. As stated in Table 3, the *e/a* value of the quasicrystal is 1.39, which is close to that (1.38) of the well-known BMG $Zr_{65}Al_{7.5}Ni_{10}Cu_{17.5}$. This implies that the *e/a* values of the ideal glass-forming compositions are also in the vicinity of this value. Six alloys with $e/a = 1.38$ were thus designed (Table 4) [75]. Bulk metallic glasses are obtained in all these compositions by suction casting in a copper mould. Thermal analysis reveals large supercooled liquid regions ΔT_x and high reduced glass transition temperatures T_{rg} values (also shown in Table 4), comparable to the well-known $Zr_{65}Al_{7.5}Ni_{10}Cu_{17.5}$ alloy under the same preparation conditions [76].

Table 3
Structure parameters and compositions of the Zr-based Hume-Rothery phases

Zr-based phase	Structure parameters (nm)	Compositions	ρ (g/cm^3)	e/a	N_v (nm^{-3})	$2k_f$ (nm^{-1})	Predominant BZ peaks	k_p (nm^{-1})
BMG-related compounds	tI-Zr_2Cu; $a = 0.3216$; $c = 1.1124$	$Zr_{66.7}Al_{1.7}N_{8.4}Cu_{22.9}$	6.750	1.28	64.4	24.81	(103)	25.89
	hP^1-Zr_6Al_2Ni (hP^2); $a^1 = a^2 = 0.8175$; $c^1 = 0.3337$; $c^2 = 0.6674$	$Zr_{65.4}Al_{11.7}Ni_{11.6}Cu_{11.3}$	6.750	1.45	74.1	26.26	(300)	26.65
	oP; $a = 0.8210$; $b = 1.3187$; $c = 0.3315$	$Zr_{65.4}Al_{11.7}Ni_{11.6}Cu_{11.3}$	6.750	1.45	74.1	26.26	(330)	26.65
	cF-Zr_2Ni; $a = 1.23$	$Zr_{67.9}Al_{5.1}Ni_{15.2}Cu_{11.8}$	6.750	1.29	65.8	24.97	(333); (511)	26.54; 26.54
Quasicrystal-related compounds	Icosahedral; $a_R = 0.5359$	$Zr_{69.5}Al_{7.5}Ni_{11}Cu_{12}$	6.750	1.39	71.0	25.61	(18/29); (20/32)	24.83; 26.11
	Icosahedral; $a_R = 0.520$	$Ti_{45}Zr_{38}Ni_{17}$	6.031	1.25	68.6	25.29	(18/29); (20/32)	25.59; 26.91
	b.c.c.-W phase; $a = 0.1432$	$Ti_{44}Zr_{40}Ni_{16}$	6.037	1.26	68.4	25.31	(530); (600)	25.59; 26.33
Elemental Zr	oP-Zr; $a = 0.512$; $b = 0.573$; $c = 0.323$	$Zr_{99}Al_1$	6.51	1.43	89.1	24.52	(200)	24.52
Zr-based BMG	BMG	$Zr_{65}Al_{7.5}Ni_{10}Cu_{17.5}$	6.750	1.38	71.6	25.67	$2\theta = 36.39^\circ$	25.30

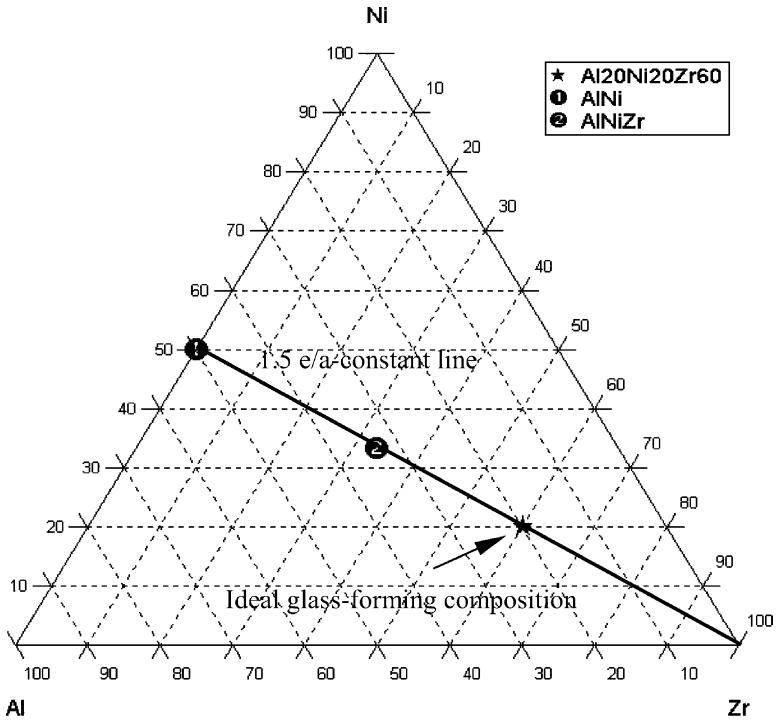

Fig. 14. The *e/a*-constant line in the Zr–Al–Ni system. The composition $Zr_{60}Al_{20}Ni_{20}$ with the largest GFA lies on this line.

From the results obtained so far, the e/a criterion seems promising. However, other criteria must be used in conjunction to pin-point the composition with the largest GFA in a given multicomponent alloy system. A possible solution is to encompass atomic size factor into the composition rules of BMGs and this attempt is in progress [75].

2.1.4. Structure of BMG

One of the general guiding principles to designing alloys that form bulk metallic glasses is to pick elements with large differences in sizes leading to a complex structure which crystallizes less

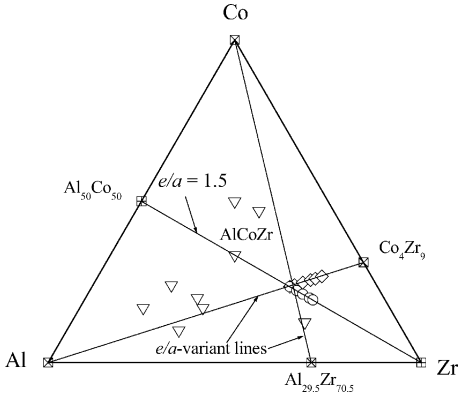

Fig. 15. Composition chart of the Zr–Al–Co system. The $e/a = 1.5$ line and two e/a-variant lines, namely, Co_4Zr_9–Al and $Al_{29.5}Zr_{70.5}$–Co, are plotted. The optimum glass-forming composition is located at the intersection point of these line: (▽) phase compositions; (◇, ○) designed compositions. [73].

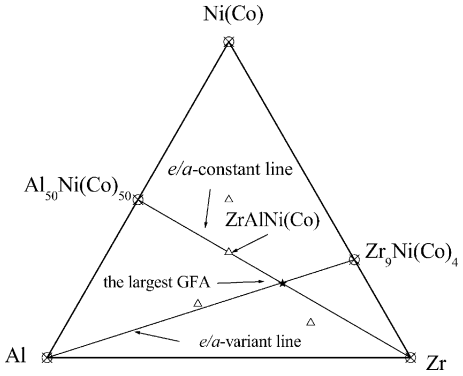

Fig. 16. The *e*/*a*-constant line Al_{50}(Ni or Co)$_{50}$–Zr and the e/a-variant line Zr_9(Ni or Co)$_4$–Al in the Zr–Al–(Ni or Co) composition chart: (△) ternary phase compositions [74].

easily. A beryllium atom, for example, is much smaller than a zirconium atom [20]. The BMGs were found to have new type of glassy structure with high degree of dense randomly packed atomic configurations. They also have new local atomic configurations, which are different from those of the corresponding crystalline phases, and long-range homogeneity with attractive interaction [77]. Density measurements show that the density difference between BMG and fully crystallized state is in the range 0.3–1.0% [78,79], which is much smaller than the previously reported range of about 2% [80] for ordinary amorphous alloys. Such small differences in values indicate that the BMGs have higher dense randomly packed atomic configurations. The reduced density function studies of the typical BMG [80–82] structures show that neither splitting of the second peak nor pre-peak at the lower wave vector is seen in the reduced density function curve of the BMG which is similar to that of the liquid alloys. This result also confirms that the multicomponent BMG has a homogeneously mixed atomic configuration corresponding to a higher degree of dense random packing. The changes of the reduced density function curve induced by crystallization indicates that the crystallization have significant effect on the chemical and topological configurations of the alloy. Such significant change implies the necessity of long-range atomic rearrangements for crystallization as well as the difference in the local atomic configurations between the amorphous and crystalline phases [80–82].

Inoue classified the BMGs into three types, namely, metal–metal-type alloys, metal–metalloid-type alloys and the Pd–metalloid-type alloys [16]. The configurations are different among the three types of BMGs as shown in Fig. 17.

In the metal–metal alloy, high-resolution TEM, XRD, and neutron diffraction studies reveal that the glass consists of icosahedral clusters [83–85]. The critical size for a transition from icosahedral cluster to icosahedral phase is around 8 nm [16]. When the BMG is annealed in supercooled liquid region, the icosahedral quasicrystalline phase (I-phase) precipitates in the primary crystallization

Table 4
Six BMGs with $e/a = 1.38$ and their thermal parameters in relation to their thermal stabilities and GFAs

Alloy compositions	T_g (K)	T_x (K)	ΔT_x (K)	T_m (K)	$T_{rg} = T_g/T_m$
$Zr_{65.5}Al_{5.6}Ni_{6.5}Cu_{22.4}$	636	733	97	1089	0.584
$Zr_{65.3}Al_{6.5}Ni_{8.2}Cu_{20}$	640	745	105	1089	0.588
$Zr_{65}Al_{7.5}Ni_{10}Cu_{17.5}$	650	750	100	1093	0.594
$Zr_{64.8}Al_{8.3}Ni_{11.4}Cu_{15.5}$	653	752	99	1085	0.602
$Zr_{64.5}Al_{9.2}Ni_{13.2}Cu_{13.1}$	658	757	99	1090	0.604
$Zr_{63.8}Al_{11.4}Ni_{17.2}Cu_{7.6}$	671	758	87	1100	0.610

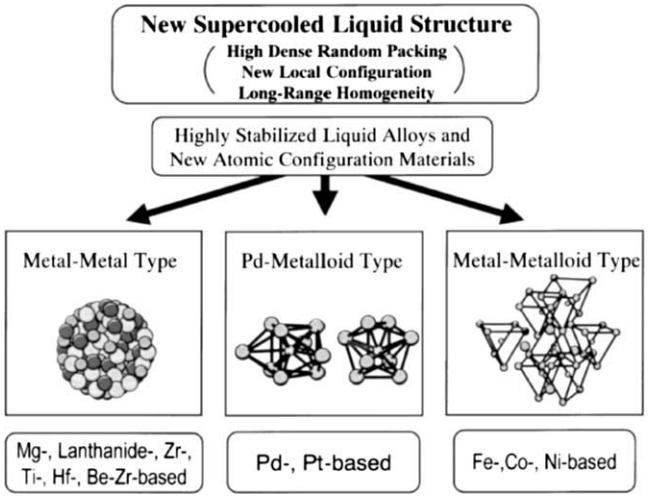

Fig. 17. The different atomic configurations of three types of BMGs [77]. (Copyright (2002) by The Japan Institute of Metals.)

step, and the I-phase transforms to stable crystalline phases at higher temperatures [83–86]. The precipitation of I-phase is structural heredity of the local structure of the BMG. The existence of icosahedral clusters provides seeds for the precipitation of the I-phase and indicates the importance of the icosahedral clusters as the fundamental structural unit. Analysis based on nucleation theory revealed that the activation energy for nucleation of I-phase is smaller than that for nucleation of crystals in the undercooled alloy melt [87].

The structure features provide a reasonable explanation to the excellent GFA of BMG forming alloys. The conventional metallic glasses with poor GFA have their corresponding crystalline compounds similar to the amorphous alloys in their local structures and compositions [88]. For these alloys, the cooling rates are the most important factor to inhibit the nucleation and growth of the competing crystalline phases. For the BMG formers, however, the critical cooling rates are much lower, and their local microstructural characterization therefore becomes a decisive factor for its glass-forming ability. The icosahedral clusters (or icosahedral short-range order) in the amorphous state would provide an additional barrier for the nucleation of the crystalline phases. Since the I-phase with five-fold rotational symmetry would be incompatible with the translational symmetry of normal crystalline phases, therefore it has to be dissociated before the formation of the crystalline phases could occur. From kinetics point of view, the crystallization of BMG requires a substantial redistribution of the component elements across the icosahedral liquid. The highly dense, randomly packed structure of the BMG in its supercooled state results in extremely slow atomic mobility [78], thus making the redistribution of atoms on a large scale very difficult. This fundamental structural discontinuity between the crystalline and the amorphous state suppresses the nucleation and growth of the crystalline phase from the supercooled liquid and results in an excellent GFA.

For the metal–metalloid-type glassy alloys, for instance Fe(Co)–Nb–B, a network atomic configurations consisting of trigonal prisms which are connected with each other through glue atoms comprising Zr, Nb, Ta or lanthanide metal are commonly found. Fe-based BMGs form primary crystals of complex f.c.c.-$Fe_{23}B_6$ phase with large lattice parameter of 1.1 nm and a unit volume consisting of 96 atoms [77].

Pd-based BMGs do not satisfy the three empirical rules proposed by Inoue, and the structural investigation shows that Pd–Cu–Ni–P BMGs consist of two large clustered units of a trigonal prism

caped with three half-octahedra for the Pd–Ni–P and a tetragonal dodecahedron for the Pd–Cu–P region, as shown in Fig. 17. As is evident from the distinctly different GFA between PdNiCuP and Pd–Ni–P, the coexistence of the two large different clustered units seems to play an important role in the stabilization of the supercooled liquid for the Pd-based alloy. This is in turn attributed to the strong bonding nature of metal–metalloid atomic pairs in the clustered units and the difficulty of rearrangement among the two kinds of clustered units.

Based on the above discussions, in summary, the bulk metallic glass-forming liquids are alloys with typically 3–5 metallic components that have a large atomic size mismatch and a composition close to a deep eutectic. They are dense liquids with small free volumes and high viscosities which are several orders of magnitude higher than those in pure metals or previously known alloys. An electronic configuration leading to a certain value of conduction electron density (e/a) add another stabilization effect of the glassy state. In the microstructure, they have unique atomic configurations which are significantly different from those for conventional metallic glasses. Thermodynamically, these melts are energetically closer to the crystalline state than other metallic melts due to their high packing density in conjunction with a tendency to develop short-range order. These factors lead to slow crystallization kinetics and high glass-forming ability of BMG formers.

2.2. Crystallization of BMGs

In order to understand the origin of the high thermal stability and excellent glass-forming ability, it is very important to clarify the crystallization behaviors of the supercooled liquid. BMGs with very stable supercooled liquid state and high thermal stability against crystallization offer a large experimentally accessible time and temperature window to investigate the nucleation and growth of crystals under various conditions in the supercooled liquid state. Extensive investigations of the crystallization process in BMG were carried out, and a lot of interesting features were reported. The results are important for a number of aspects, namely, the understanding of the nucleation and growth in the metallic supercooled liquid, the evaluation of the glass-forming ability of the melts and the thermal stability of metallic glasses, as well as the production of bulk nanocrystalline and composites from controlled crystallization [89–102].

Vitalloys and PdNiCuP have been studied to extensively. The common features of the nucleation and growth in BMG supercooled liquids are high number density of nuclei and sluggish growth kinetics [89–95]. The number of nucleation events was found to increase from 10^8 m^{-3} for samples annealed near melting temperature to 10^{23} m^{-3} for samples annealed in the vicinity of T_g. The crystallization at low temperature (near T_g) requires a large number of pre-existing nuclei. One single concept of nucleation mechanism normally cannot provide an adequate description of the nucleation process in the whole supercooled liquid region. Other mechanisms such as extremely high heterogeneous nucleation rates, quenched-in nuclei, phase separation in the supercooled liquid prior to crystallization, or a homogeneous nucleation model taking into account linked fluxes of interface attachment and diffusion in the liquid to the cluster neighborhood were applied to describe the high density of nuclei [89–102]. Another feature is that the locations of the maxima in nucleation rate and growth rate are very different. In vit1, the growth rate maximum locates at 985 K, which is much higher than that of the nucleation rate at 840 K [91]. Therefore, the nuclei formed in supercooled liquid have marked different growth rates during constant heating and cooling at ambient condition for the alloy. A rate of about 10 K/s is sufficient to suppress crystallization in the supercooled liquid and get full amorphous phase in the quenching process. In contrast, a heating rate of about 200 K/s is necessary to avoid crystallization in the amorphous state as shown in Fig. 18.

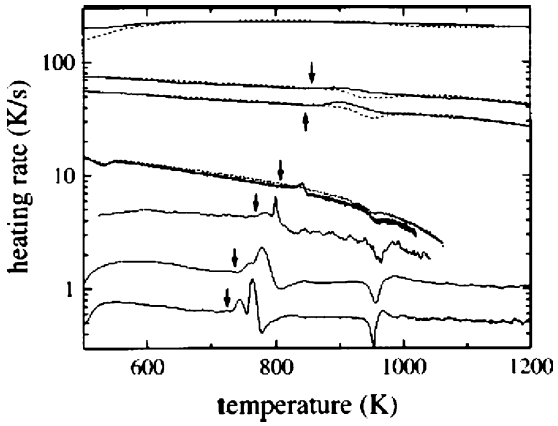

Fig. 18. Derivative of the temperature–time profile, recorded during heating of amorphous (solid line) and crystalline (dashed line) vit1 vs. temperature. The onset of recoalescence is marked by arrows [91]. (Copyright (1999) by the American Physical Society.)

2.3. *Effects of high pressure*

With the development of high pressure techniques, pressure is becoming an important processing variable just like that of temperature or chemical composition for condensed phases. High pressure (HP), which can cause a larger change of atom spacing, chemical bonding and Gibbs free energy, has been found to be a powerful tool for affecting and controlling the nucleation and growth in the metallic glasses [103,104]. For example, since high pressure can promote local atomic rearrangement and suppress the long-range atomic diffusion in supercooled liquid state, BMGs can be crystallized under HP to very fine-grained nanostructured materials. Contamination and grain growth that often occur during consolidation of nanoparticles could be avoided in the nanostructured material derived from BMG [96].

Extensive study of the crystallization behaviors under high pressure have been performed for gaining insight into the mechanism of the nucleation and growth processes in BMGs [95,96,100,105–107]. Crystallization in BMGs is very complex due to possible phase separation before the primary crystallization and complicated diffusion fluxes in the supercooled liquid state. It also depends strongly on the heating rate, annealing time and a number of other factors. The effect of pressure on metallic glasses is complex as well. HP has been found to promote or suppress crystallization in different glasses [108,109]. For example, Shen et al. [103] found that appropriate pressure could lower or raise activation energy of the crystallization. In other words, the pressure effect on crystallization temperature T_x is not monotonous. For BMG with complicated multistage crystallization process, the effect of pressure on T_x depends on the applied pressure range and time. One thus cannot simply extrapolate or compare the effect of pressure on T_x in different pressure ranges.

Different techniques used to study the crystallization may also result in different observations. X-ray diffraction (XRD) has limited sensitivity in detecting the precipitation of nanocrystalline particles in the amorphous matrix induced by primary crystallization. High-resolution transmission electron microscope (HRTEM) and differential scanning calorimeter (DSC) are more sensitive way to detect the primary nanocrystallization. T_x determined by HRTEM and DSC is much lower than that by XRD. The most important is that the crystallization kinetics of the BMG is very sluggish, and the crystallization strongly depends on the treatment process, heating or cooling rate and annealing time. Primary nanocrystallization occurs in vit1 when annealed at 623 K (much lower than

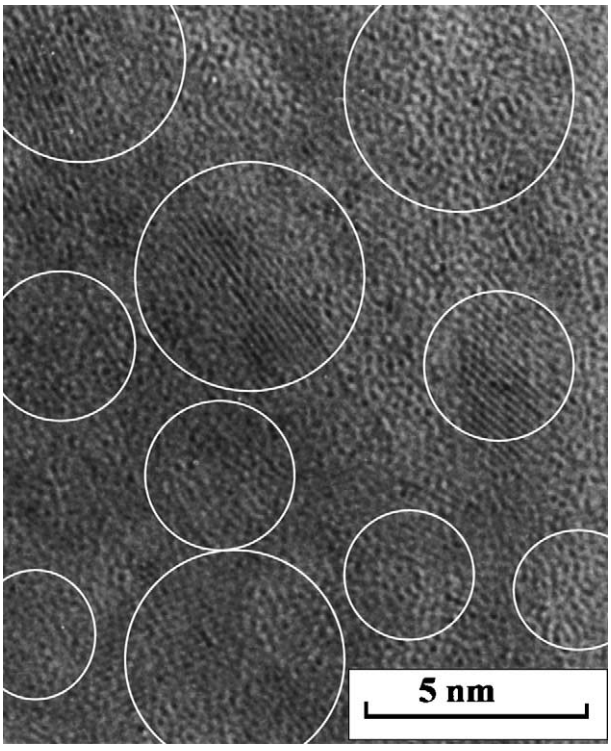

Fig. 19. The HRTEM micrograph of the vit1 BMG annealed at 623 K under 4 GPa for 4 h [96].

$T_x = 698$ K [76]) for long time at vacuum as shown in HRTEM picture of Fig. 19. The pressure treatment conditions, such as heating or cooling rate, annealing time at each annealing temperature should be considered when comparing the different crystallization behaviors of the BMG under HP. Otherwise, it could induce confusion regarding the crystallization process of BMG. Up to now, a proper understanding of the crystallization of the BMGs is still lacking. Different researchers sometime got different and even contradictory results due to their different pressure annealing conditions and detecting methods used. This makes the design of experiment and interpretation of experimental results difficult. Therefore, more work is necessary to systematically study the effects of pressure on the nucleation and growth in BMGs upon various conditions.

On the other hand, the ability to form a glass by cooling from the equilibrium liquid is equivalent to suppressing crystallization within the supercooled liquid. To better understand the GFA of metallic alloys, an important step is to develop a controlled method to examine the nucleation and growth of crystalline phases in the undercooled melt. The applied pressure can suppress the nucleation and growth of the undercooling melts, and increases the melting points of most alloys and leads to a larger undercooling of the liquid alloy. Applying a high pressure during the solidification process of a glass-forming alloy can therefore improve the GFA, and provide a useful way to study the formation mechanism of the BMGs. Fig. 20 shows the synchrotron XRD traces for the vit4 alloy cooled at a cooling rate of ~20 K/s under different pressures [105]. The samples with higher applied pressure (>6 GPa) show a broad scattering peak indicating the full amorphous phase can be obtained. However, when quenching at lower pressure (4.5 GPa), there are a few weak but sharp crystalline peaks superposing on the broad hump meaning that full amorphization cannot be attained at this pressure. When cooling at much lower pressure (2.5 GPa), more sharp crystalline peaks are superposing on the broad peak with a volume fraction of crystalline phases estimated to be more than

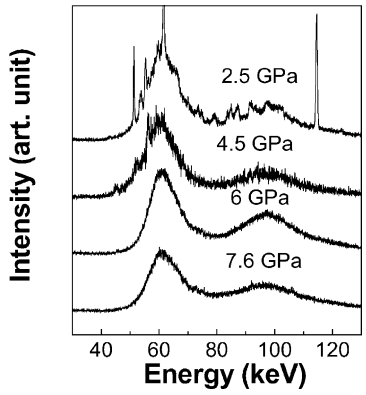

Fig. 20. The synchrotron XRD traces for the vit4 alloy cooled at a cooling rate of ∼20 K/s under different pressures [105].

15%. The sample cooled with a similar cooling rate (∼20 K/s) at ambient pressure consists of mostly crystalline phases [110]. In the experiments, the heterogeneous nucleation environments are identical for all the samples cooled with different applied pressures. XRD result indicates that the GFA of vit4 is enhanced under high pressure since pressure can lead to the annihilation of the free volume, reduce voids through compressing the melt structure and increase the viscosity of the melt during the solidification process. Nucleation is more difficult, and the subsequent growth of the successful nuclei is inhabited by the extremely low atomic mobility. The increased GFA of the alloy under high pressure also confirms that the kinetic factor such as atomic mobility and viscosity of the melt is the key factor in the formation of BMGs.

3. Properties and behaviors of BMG

In addition to the importance to basic sciences, BMGs have some excellent physical and chemical properties which are promising for applications. We focus here on the mechanical, magnetic and acoustic properties of the BMGs. We also introduce the properties and behaviors of BMG under some extreme conditions.

3.1. Mechanical properties

Fig. 21 summarizes the relationship between Young's modulus (E) and tensile fracture strength ($\sigma_{t,f}$) or Vickers hardness (H_v) for typical BMGs [111,112]. It can be seen that the tensile fracture strength and H_v have a roughly linear relationship with E, which can be expressed as follows: $\sigma_{t,f} = 0.002E$, and $H_v = 0.06E/9.8$. For vit1, $E = 90$ GPa, $\sigma_{t,f} = 1.9$ GPa [11,113]. The slope of 0.002 corresponds to an elastic strain limit of the BMGs. A similar trend is also evident for ordinary crystalline alloys shown in the figure, but the slopes of the linear region for the BMGs are much steeper than that for the crystalline alloys, indicating the larger elastic limits of the BMGs compared with those of the crystalline alloys [114,115]. The much better linearity of the lines for BMGs is attributed to the formation of an ideally homogenized solid solution over the whole composition range which is one of the typical features of glassy alloys.

It can be summarized that BMGs have much higher tensile strengths and much lower Young's moduli. The difference in these values between the BMG and crystalline alloys is as large as 60%. The significant difference in the mechanical properties is thought to be a reflection of the difference

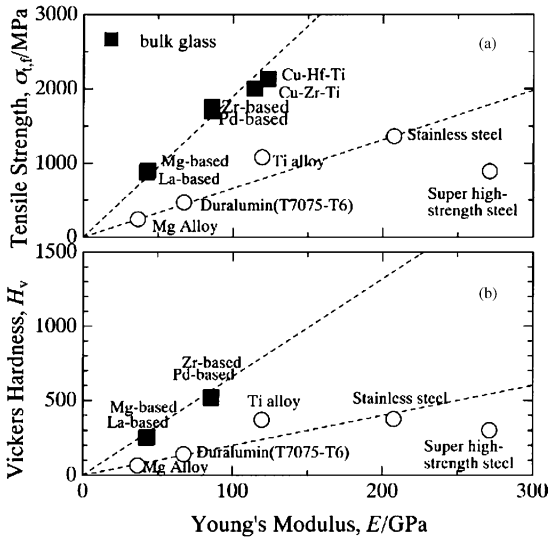

Fig. 21. The relations between mechanical properties of typical BMGs: (a) tensile fracture strength ($\sigma_{t,f}$) with Young's modulus (E); (b) Vickers hardness (H_v) with Young's modulus (E) [77]. (Copyright (2002) by The Japan Institute of Metals.)

in the deformation and fracture mechanisms between BMGs and crystalline alloys. Plastic deformation in metallic glasses is generally associated with inhomogeneous flow in highly localized shear bands. Fractographic evidence in Figs. 22 and 23 from tensile experiments strongly suggests that under high strain rate conditions, local melting occurs during unstable fracture. Even under slower loading rates, a veined fracture surface indicates a decrease in the glass viscosity. Due to the

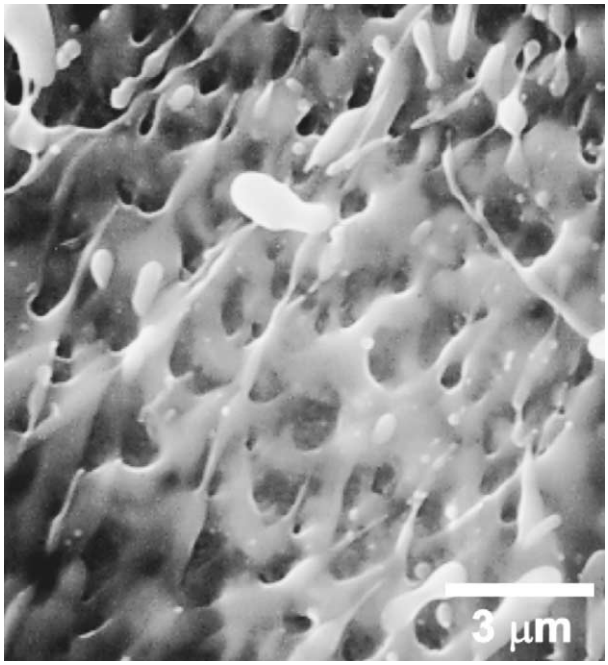

Fig. 22. Failure surface from a tensile sample which exhibited cup- and cone-type fracture. The droplets are indicative of localized melting under the higher strain rates associated with this experiment.

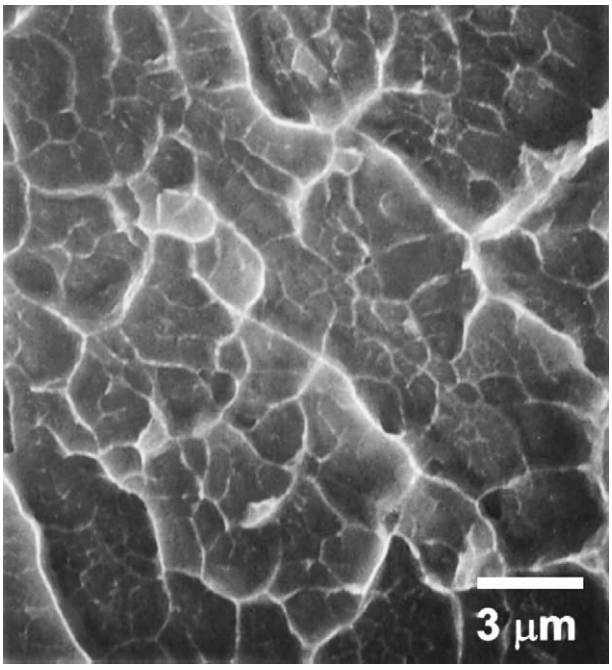

Fig. 23. Fracture surface from a typical fracture toughness experiment. The vein pattern suggests a decrease in the glass viscosity resulting in highly localized flow processes on the crack plane.

highly localized nature of flow and the lack of microstructural features in the metallic glass to divert the flow, shear band formation typically leads to catastrophic failure. The localization of shear is associated with possible strain-softening mechanisms and thermal softening as well as the absence of strain-hardening (working hardening) mechanisms. In fracture toughness measurements using a single-edge notched tension sample for modifying the plastic strain field at the crack tip, a stable damage zone of branched cracks is formed (see Fig. 24). This damage zone is well contained within the classical plastic zone. By modeling the crack branches as an array of parallel cracks in an infinite plate, the cracks grow at local stress intensity of 10–15 MPa/m, which is in good agreement with the

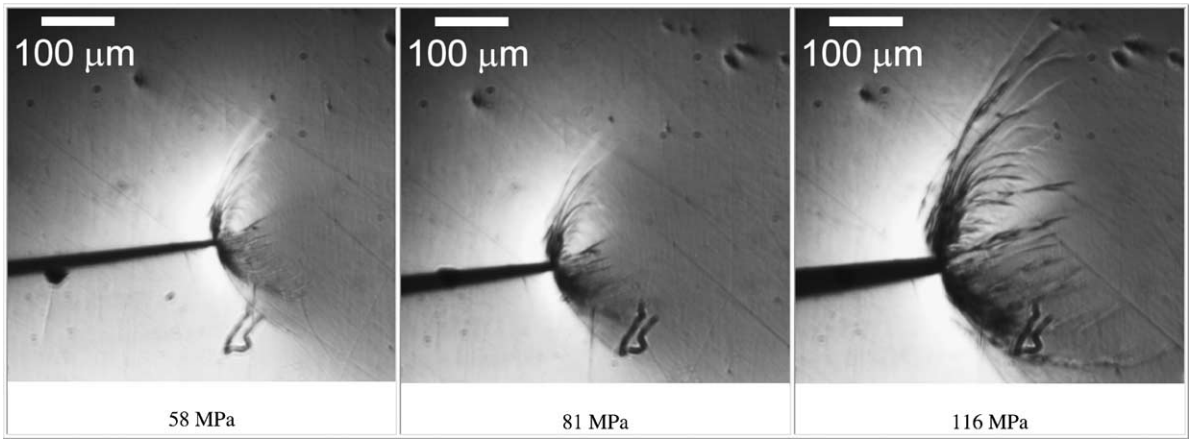

Fig. 24. In situ images of crack tip branching in a single-edge notched tension sample during a fracture toughness experiment. The stress intensities refer to the main crack tip.

meniscus instability model. The obvious softening of the fracture surface has led several researchers to conclude that shear band formation is associated with localized heating [11]. In addition to the heating associated with plastic deformation, a cooling zone is visible ahead of the crack tip. This is consistent with thermoelastic cooling effects. Under tensile load, there is little global plasticity of the sample as a whole, but geometrical confinement of shear bands can dramatically enhance overall plasticity [11].

In addition to the high static mechanical strength, the Zr-based BMGs exhibit high Charpy impact fracture energies ranging from 110 to 140 kJ/m^2 and high fracture toughness limit [77]. The fatigue limit is nearly the same as those of the crystalline alloys. Considering that the tensile fracture strength of the BMG is about double that of the crystalline alloys, the fatigue endurance stress level is also much higher for the BMGs. It is also found that the difference in BMG and crystalline structure does not play a dominant role in the propagation velocity of fatigue cracks, though the deformation and fracture behavior under a uniaxial applied load is markedly different from those for crystalline alloys [77].

In contrast to metallic glasses, useful crystalline metals exhibit substantial plastic strains following yielding under tension, and this results in high fracture toughness and impact resistance. However, BMGs usually are ''brittle'' and exhibit no plasticity [11]. Fatigue and fracture toughness tests of Vitreloy, however, seem to cast some doubt on the new material's prospects for future use in tougher, industrial-type applications that require long-term performance beyond that demanded by sporting goods. It is confirmed that the glassy metal has high fracture toughness, but minute amount of crystallization of the material causes a dramatic drop in toughness. This could mean that applications at temperatures above the glass-transition temperature are limited, at least regarding long-term applications. Furthermore, standard stress–strain fatigue tests show that Vitreloy has an extremely low resistance to crack initiation and a crack propagates rapidly once it has formed. If this alloy does start to yield or fracture, it fails quickly. Geometrical confinement of shear bands can dramatically enhance overall plasticity [11]. Recent efforts on improving the plasticity have been focused on fabricating metallic glass composites. A variety of BMG composites have been formed by the introduction of reinforcing crystalline phase into the glassy matrix. Fig. 25 shows SEM backscattered electron image of in situ ZrTiNbCuNiBe composite microstructure (inset: X-ray diffraction pattern for the in situ composite) [116]. Primary dendrite growth and solute partitioning in the molten state yields a microstructure consisting of a ductile crystalline Ti–Zr–Nb β-phase, with b.c.c. structure, in a Zr–Ti–Nb–Cu–Ni–Be bulk metallic glass matrix. Fig. 26 is the compressive stress strain curve for cylindrical in situ composite specimen [97]. Total strain of over 8% is achieved prior to failure. This indicates that a ductile metal reinforced bulk metallic glass matrix composite is obtained, and the plastic strain to failure, impact resistance, and toughness of the metallic glass are all dramatically increased.

3.2. Acoustic and elastic properties

The studies of the acoustic, elastic and thermal properties of metallic glasses can provide important information about the structural and vibrational characteristics [117–119]. The equation of state (EOS) of a solid (pressure–volume relation) plays an important role in condensed matter physics, because the knowledge of the EOS is of central importance for the general understanding of the behavior and the application of condensed matters [120]. The EOS of crystalline solids has been a long-standing topic and extensively investigated. A lot of interesting and important phenomena have been observed [120]. For many years, however, the very high cooling rate (>10^5 K/s) necessary to obtain metallic glasses limits their geometry to very thin ribbons or wires, and makes the studies

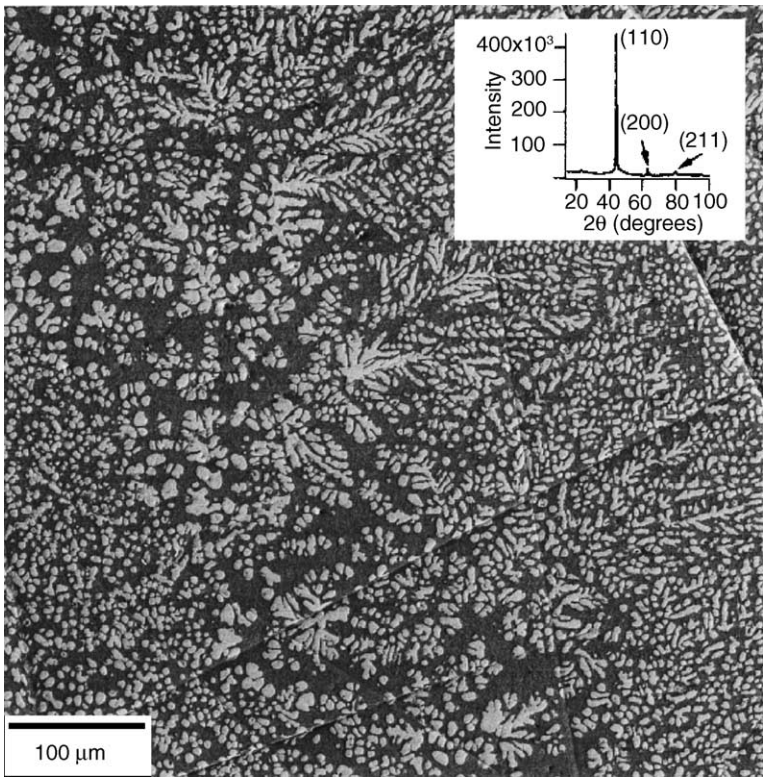

Fig. 25. SEM backscattered electron image of in situ composite microstructure (inset: X-ray diffraction pattern for the in situ composite) [116]. (Copyright (2000) by the American Physical Society.)

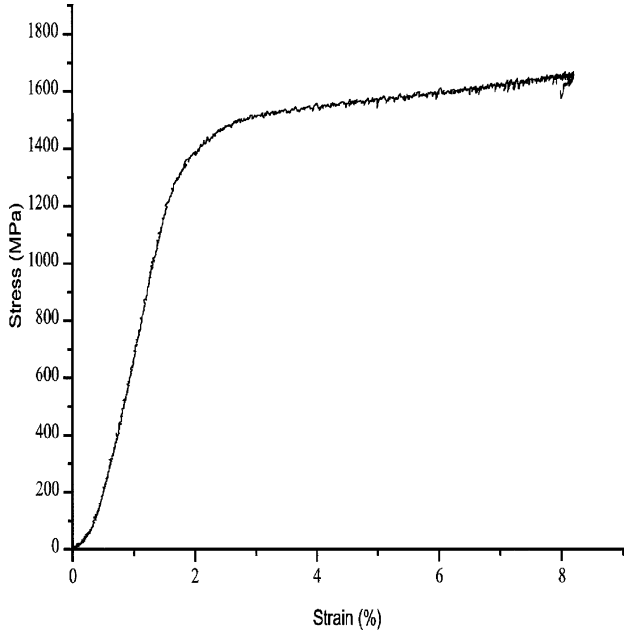

Fig. 26. Compressive stress strain curve for cylindrical in situ composite specimen [116]. (Copyright (2000) by the American Physical Society.)

of intrinsic nature of the glass and glass transition as well as the measurements of many physical properties for establishing the EOS very difficult. The experimental data about acoustic and elastic properties in the metallic glasses are scarce, and the vibrational features in the metallic glasses are poorly understood. EOS is even more difficult to obtain for the metallic glasses, because the measurements have been impeded mainly by the lack of bulk specimens.

A fundamental understanding of microstructural configuration under high pressure in amorphous solids is not as developed as that in crystalline solids. The difficulties in preparing bulk samples are, again, the main obstacle. The BMGs are in the form suitable for measurements of elastic wave propagation. The pressure and temperature dependence of the structural and physical properties of the BMGs could be investigated by the ultrasonic method. In addition to examining the fundamental elastic and thermal behaviors, ultrasonic method is also a powerful tool for studying the relationship of microstructure and properties. Since acoustic property is particularly sensitive to the microstructure, the *T*-dependent acoustic velocities can provide critical information on the micostructural characteristics and their evolution as well as the elastic and thermal properties during the glass transition of the BMG. The method is a very powerful tool for the study of the nature of glass transition, metallic glassy and supercooled liquid states. Systematic ultrasonic investigation on BMGs have been performed for studying the nature and properties of the metallic glasses and the glass transition [121–134]. The acoustic features of BMGs are measured and compared with those of other glasses. Table 5 lists the acoustic data, Debye temperature and elastic constants for typical BMGs and oxide glasses.

In Table 5, σ characterizes the relative value of the compressive and shear deformation of a solid [135]. The values of σ for various BMGs range from 0.3 to 0.4, which are close to that of crystalline metals [136], e.g. 0.37 for copper and 0.33 for Monel which is a crystalline copper alloy. On the other hand, conventional metallic glasses have higher value of σ (≈ 0.40) [137], while typical oxide glasses have σ ranges from 0.15 to 0.25 (see Table 5). The oxide glasses are brittle, since atoms or molecules can hardly rearrange themselves to shear strains without a drastic disturbance in bonding configurations. In contrast, the metallic glasses with higher value of σ have better plastic deformation indicating the ease of atomic rearrangement in the materials. The comparison indicates

Table 5
The acoustic data and elastic constants for typical BMGs and oxide glasses at ambient pressure

Sample	ρ (g/cm^3)	v_l (km/s)	v_s (km/s)	E (GPa)	G (Gpa)	K (GPa)	σ	θ_D (K)	V_l/V_s	K/G
$Zr_{41}Ti_{14}Cu_{12.5}Ni_{10}Be_{22.5}$	6.125	5.174	2.472	101	37.4	114.1	0.35	327	2.09	3.06
$Zr_{46.75}Ti_{8.25}Cu_{7.5}Ni_{10}Be_{27.5}$	6.014	5.182	2.487	100.5	37.2	111.9	0.350	327	2.08	3.01
$Zr_{45.4}Ti_{9.6}Cu_{10.15}Ni_{8.6}Be_{26.25}$	6.048	5.171	2.485	100.9	37.3	111.9	0.350	327	2.08	3.00
$Zr_{48}Nb_8Cu_{12}Fe_8Be_{24}$	6.436	4.994	2.338	95.7	35.2	113.6	0.359	306	2.13	3.22
$(Zr_{0.59}Ti_{0.06}Cu_{0.22-}Ni_{0.13})_{85.7}Al_{14.3}$	6.608	4.890	2.269	92.7	34.0	112.6	0.363	291	2.15	3.31
$Cu_{60}Zr_{20}Hf_{10}Ti_{10}$	8.315	4.620	2.108	101.1	36.9	128.2	0.368	282	2.02	3.47
$Pr_{60}Cu_{20}Ni_{10}Al_{10}$	6.900	3.030	1.406	37.2	13.6	45.2	0.363	160	2.16	3.31
$Pd_{39}Ni_{10}Cu_{30}P_{21}$	9.152	4.74	1.96	98.2	35.1	159.1	0.40	280	2.42	4.52
Float glass	2.518	5.85	3.47	74.5	30.3	45.7	0.23	320	1.69	1.5
Ti-glass	2.196	5.745	3.615	67.3	28.7	34.2	0.17	330	1.59	1.2
Window glass	2.421	5.593	3.385	67.2	27.7	38.7	0.211	–	1.65	1.40
Water-white glass	2.479	5.836	3.423	71.9	29.1	45.7	0.238	–	1.70	1.57
Fused quartz	2.201	5.96	3.75	72.7	31.0	36.9	0.17	496	1.59	1.16
Microcrystal glass	2.556	6.490	3.666	87.0	34.4	61.9	0.266	–	1.77	1.80
Borosilicate glass	2.32	5.64	3.28	61.90	24.9	40.52	0.24		1.72	1.6
Carbon glass	1.56	3.88	2.407	21.4	9.01	11.4	0.187	338	1.61	1.26

that σ bears certain relationship with the atomic configuration in these amorphous materials. The GFA also has relation with the value of σ of a glass-forming system. The conventional metallic glasses have poor GFA (the critical cooling rate, R_c, for the glass formation, which represents the GFA of an alloy, is from 10^4 to 10^7 K/s). The GFA of the BMGs (R_c ranges from 1 to 100 K/s; for vit1, R_c is even lower than 1 K/s [11]) is much better than that of the conventional metallic glasses and approaches that of the oxide glasses whose R_c is less than 1 K/s. A smaller σ may result in high GFA in a glass-forming system.

The nature of the chemical bonds in a solid determines the microstructure of the solid, thus the difference in microstructure will influence the mechanical properties of a solid and then result in the variation of the acoustic parameters. Comparing with oxide glasses, BMGs have large values of E, K, G and K/G. K/G are between 1.16 and 1.8 for the covalent bond oxide glasses and 3.0 and 4.5 for various BMGs which is similar to metals, such as Cu and steel (K/G is about 2.5) [136] and markedly different from those of oxide glasses. The relatively larger values of G and E for the BMG compared to oxide glasses means that the bond length and bond angle of the structure in the BMGs cannot be changed easily. Acoustic results confirm the different microstructural characteristic between the two kinds of glasses.

The temperature- and pressure-dependence of the density and acoustic velocities were measured to reflect the microstructural change during transformation and application of pressure. Fig. 27 presents the pressure dependence at 20 MHz of v_l and v_s, $\Delta v(P)/v(P_0) = [v(P) - v(P_0)]/v(P_0)$, where P_0 is the ambient pressure, of the vit1 BMG. The data of v_l and v_s are reproducible and show no measurable hysteresis effects in the pressure loading and release cycle. It seems that there are no observable permanent changes in acoustic velocities up to 2.0 GPa. No detectable density increase in the sample after testing was found. These results indicate the perfectly elastic behavior in the BMG under hydrostatic compression up to 2.0 GPa. The change of v_l upon pressure is two times larger than that of the v_s. Both v_l and v_s increase smoothly with increasing pressure and show an approximately linear P-dependence.

For comparison, Fig. 28 shows the pressure variations at 20 MHz, $\Delta v(P)/v(P_0) = [v(P) - v(P_0)]/v(P_0)$, of v_l and v_s of the typical silicate Ti-glass (oxide glass of $SiO_2 + 8.4$ wt.% TiO_2 glass). Similar to that of BMG, the data of v_l and v_s are reproducible in the pressure loading and release cycle and show no measurable hysteresis effects. However, in contrast to BMG, v_l and v_s of the silicate glass decrease almost linearly with increasing P. This indicates that oxide glass with covalent atomic structure has different response to pressure compared to that of BMG (with dense random

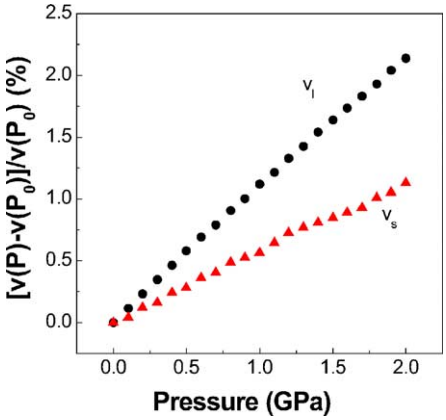

Fig. 27. Variation of longitudinal and transverse velocities ($v = v_l, v_s$) of the $Zr_{41}Ti_{14}Cu_{12.5}Ni_{10}Be_{22.5}$ BMG upon pressure at room temperature. v is normalized by $\Delta v/v_0 = (v - v_0)/v_0$, where v_0 is a normal velocity at ambient pressure P_0.

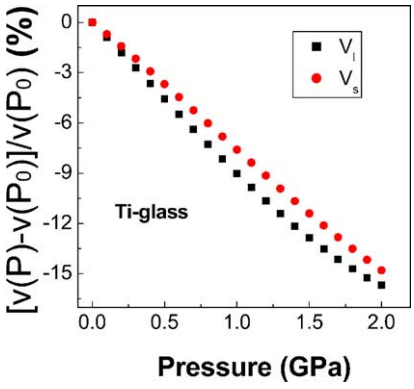

Fig. 28. Variation of longitudinal and transverse velocities ($v = v_l, v_s$) of the Ti-glass upon pressure at room temperature. v is normalized by $\Delta v/v_0 = (v - v_0)/v_0$.

packed structure) [138]. The corresponding P-dependence of elastic constants Y ($Y = E$, G, K, σ) calculated from the velocities for vit1 and Ti-glass are shown in Figs. 29 and 30, respectively. Y is normalized by $\Delta Y/Y_0 = (Y - Y_0)/Y_0$, where Y_0 is a normal modulus at P_0. For the BMG, E, G, K and σ increase monotonically and linearly with increasing pressure. In the absence of phase changes, such an increase with increasing pressure is generally expected as a consequence of the vibrational anharmonicity of the BMG [139]. dK/dp of vit1 is positive, i.e. the elastic constants exhibit a positive deviation with pressure from linearity, showing that the BMG stiffen under hydrostatic pressure. The monotonic increases of K can be attributed to the denser packing of the BMG. The application of pressure does not induce acoustic mode softening for the BMG.

For Ti-glass, E G, K and σ decrease monotonically and nonlinearly with increasing pressure. At higher pressure, especially K and σ show obviously nonlinear behavior upon P, and $\mathrm{d}K/\mathrm{d}p < 0$, indicating pressure induce acoustic mode softening. This is markedly different from that of BMG. The pressure leads to a smaller change of v_s (1.2%) and G (4.1%), and relatively larger changes of v_l (2.2%) and K (7.1%) (listed in Table 6). This result means that pressure has larger effect on the longitudinal acoustic phonons than the transverse phonons in the BMG. Crystallization causes obvious stiffening of transverse acoustic phonons relative to the BMGs [79]. Table 7 exhibits the acoustic and elastic parameter changes after crystallization in vit1. The changes are not simply attributed to the small

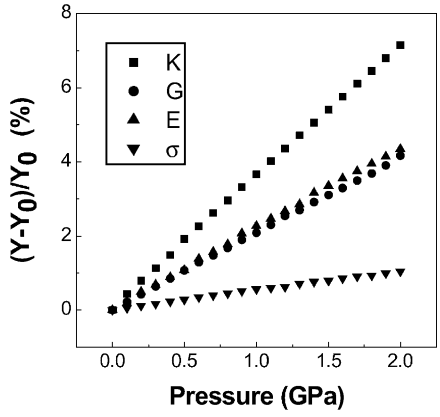

Fig. 29. The variation of elastic constants Y of the $Zr_{41}Ti_{14}Cu_{12.5}Ni_{10}Be_{22.5}$ BMG ($Y = E$, G, K, σ) with pressure, Y is normalized by $\Delta Y/Y_0 = (Y - Y_0)/Y_0$, where Y_0 is a normal modulus at P_0.

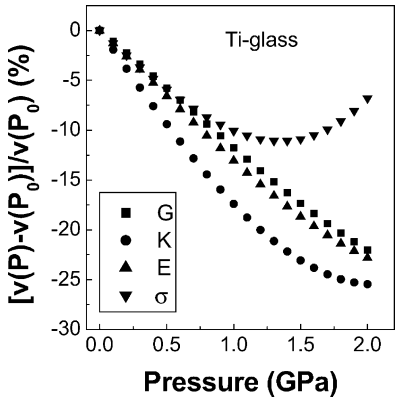

Fig. 30. The variation of elastic constants Y of the Ti-glass ($Y = E$, G, K, σ) with pressure, Y is normalized by $\Delta Y/Y_0 = (Y - Y_0)/Y_0$, where Y_0 is a normal modulus at P_0.

Table 6
A comparison of properties at ambient state (Y_0) and under high pressure (Y_p) of the vit1 and Ti-glass

Property	Vit1			Ti-glass		
	Ambient pressure	2 GPa	$(Y_p - Y_0)/Y_0$ (%)	Ambient pressure	2 GPa	$(Y_p - Y_0)/Y_0$ (%)
v_l (km/s)	5.174	5.297	2.2	5.757	4.844	−15.7
v_s (km/s)	2.472	2.501	1.2	3.615	3.080	−14.8
K (GPa)	114.1	122.9	7.1	34.2	25.5	−25.4
G (GPa)	37.4	39.0	4.1	28.7	22.4	−22.0
θ_D (K)	326.8	332.8	1.8	330.0	280.1	−15.1

density difference between the amorphous and crystalline states. Instead, it is mainly related to the unique microstructural characteristics of the metallic glassy state instead. The softening may have close link with the excellent glass-forming ability of the glass-forming system [125].

The Grueneisen constant γ, which is related to the derivative of K, can be estimated by using the Slater's equation [140]:

$$\gamma = \frac{1}{2}\left(\frac{\partial K}{\partial p}\right)_T \tag{3.1}$$

The value of γ of vit1 is 2.0 as estimated from Fig. 3. For Ti-glass, the value of γ is −4.02 as estimated from Fig. 29. The values are close to the reported values of fused silica (−2.9) [141], etched soda glass (2.5) [141], iron (3.4) [142] and silicon (0.8 to −1.5) [143]. This classifies the BMG among the solids with larger anharmonicity.

Table 7
A comparison of the properties of metallic glasses state (Y_a) and fine-grained crystallized state (Y_c) of $Zr_{41}Ti_{14}Cu_{12.5}Ni_{10}Be_{22.5}$ alloy

Alloy	ρ (g/cm^3)	v_l (km/s)	v_s (km/s)	K (GPa)	G (GPa)	$\theta_D(T)$ (K)
Glassy state	6.125	5.174	2.472	114.1	37.41	326.8
Crystallized state	6.192	5.446	2.807	118.6	48.8	370.9
$(Y_c - Y_a)/Y_a$ (%)	1.1	5.2	13.5	3.9	30.3	13.4

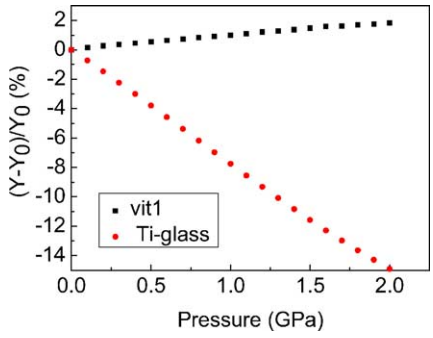

Fig. 31. The relative variation of the Debye temperature, θ_D of vit1 and Ti-glass with pressure, Y is normalized by $\Delta Y/Y_0 = (Y - Y_0)/Y_0$, where Y_0 is a normal Debye temperature at P_0.

The Debye temperature θ_D, representing the temperature at which nearly all modes of vibrations in a solid are excited [144], can also be determined from acoustic data with the equation [144]:

$$\theta_D = \frac{h}{k}\left(\frac{4\pi}{9}\right)^{-(1/3)} \rho^{1/3}\left(\frac{1}{v_l^3} + \frac{2}{v_s^3}\right)^{-(1/3)} \tag{3.2}$$

where k is Boltzmann's constant and h the Planck constant. The pressure variation of θ_D reflects the rigidity of a solid change with pressure. Fig. 31 shows the pressure variation of θ_D for vit1 and Ti-glass in the range of 0–2 GPa. For the BMG, θ_D increases monotonically and slightly with increasing pressure, implying an increase in rigidity of the BMG with pressure [145]. While for Ti-glass, θ_D decreases monotonically and significantly with increasing pressure, meaning that the rigidity of the oxide glass is very sensitive to pressure and decreases rapidly with increasing pressure. In contrast to that of vit1, large changes in v_s (−15.7%), v_l (−14.8%), K (−25.4%), G (−22.0%) and θ_D (−15.1%) under 2 GPa occur (listed in Table 6). Pressure induces obvious softening of acoustic phonons relative to Ti-glass at ambient condition.

The different responses to pressure of silicate and metallic glasses are due to completely different structural characteristic of BMGs (random close packing (r.c.p.) atomic configuration) and oxide glasses (continuous-random networks (c.r.n.)). Oxide glass is a covalent-bonded glass with a significant spread in Si–O–Si bond angles. Under high pressure, the change of the bond angles between atoms in oxide glass leads to negative pressure-dependent velocities. For BMGs with r.c.p. structure, however, the nature of metallic bond is retained in the BMGs, although atomic long-range order is lacking. In the transition process from the glass to crystalline state, there is no significant change of the nearest-neighbor atoms and the distance between atoms. However, the small change of the volume can sensitively induce changes in the electron configuration, atomic interaction force and the relative flow between atoms. So BMGs have a large shear modulus change upon crystallization.

From the data of K_0 and K_0' (K_0 and K_0' are the bulk modulus and its pressure derivation at P_0, respectively), the volume compression $V_0/V(P)$ and their hydrostatic pressure dependence, or the equation of state of the BMG and Ti-glass in the non-phase transitional case, are obtained using the Murnaghan form [146]:

$$P\,(\mathrm{GPa}) = \left(\frac{K_0}{K_0'}\right)\left[\left(\frac{V_0}{V(P)}\right)^{K_0'} - 1\right] \tag{3.3}$$

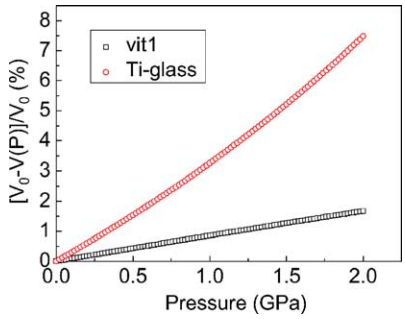

Fig. 32. A comparison of the pressure and volume relation of the vit1 and Ti-glass.

The P–V relation of the BMG and Ti-glass are plotted in Fig. 32. The obtained EOS of vit1 is close to that obtained by direct P–V measurements at room temperature [147]. Comparing with oxide glass the Zr-based BMGs exhibits much smaller volume change upon P as shown in Fig. 32. The volume compressibility of metallic elements can be expressed as [148]

$$\frac{\Delta V}{V_0} = -aP + bP^2 \tag{3.4}$$

where a and b are constants, and volume compression $\Delta V = V(P) - V_0$. For comparison, the compression curves of Zr, Ti, Cu, Ni and Be obtained by directly volume and pressure measurements [148] are also plotted in Fig. 33. The compression curves of the BMG is interposed among their metallic components, e.g. the compression curve of the $Zr_{41}Ti_{14}Cu_{12.5}Ni_{10}Be_{22.5}$ BMG is interposed among Zr, Ti, Cu, Ni and Be. To understand the phenomenon, the volume compression of the BMG is calculated as a mean value of all elements based on the atomic percents of constituent elements. The calculating result is also shown in Fig. 33. The calculating EOS for vit1 in terms of Eq. (3.4) agrees well with its EOS derived from the Murnaghan form and experimental data (Eq. (3.3)). This phenomenon has been found in a series of acoustic measurement for various BMGs as shown in Fig. 34 [127]. This indicates that the compression curves of the BMG has correlation with that of their metallic components and exhibit a roughly weighted average of these elements. Since the compressibility of a solid is determined by the nature of the interatomic potential and the atomic

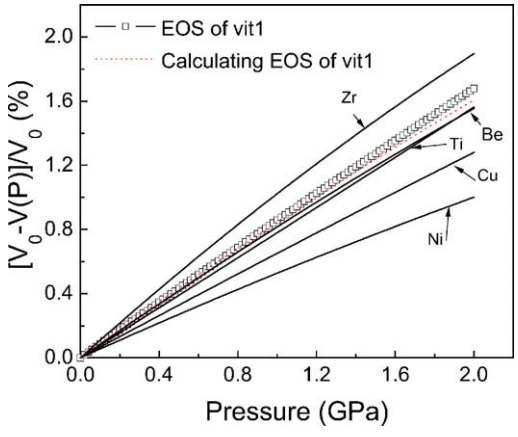

Fig. 33. The pressure and volume relation of the BMG got from acoustic measurement, a comparison of the EOS of vit1 and its crystalline components.

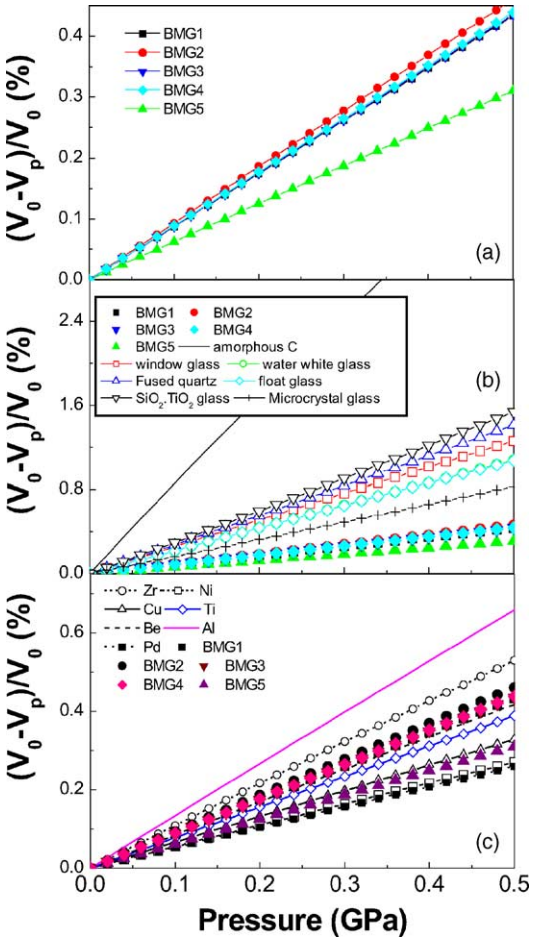

Fig. 34. The pressure and volume relation of the BMGs: (a) EOS of the BMGs [$Zr_{41}Ti_{14}Cu_{12.5}Ni_{10}Be_{22.5}$ (BMG1), $Zr_{41}Ti_{14}Cu_{12.5}Ni_9Be_{22.5}C_1$ (BMG2), $Zr_{48}Nb_8Cu_{12}Fe_8Be_{24}$ (BMG3), $Zr_{50.6}Ti_{5.2}Cu_{18.8}Ni_{14.1}Al_{14.3}$ (BMG4) and $Pd_{39}Ni_{10}Cu_{30}P_{21}$ (BMG5)]; (b) a comparison of the EOS of silicate glasses and BMGs; (c) a comparison of EOS of crystalline components and BMGs [114].

configurations, the total compression of BMGs can be ascribed to the contribution of individual metallic elements. The above results therefore imply that the short-range order structure of the BMG has close correlation with the atomic configurations in their metallic components. Since those metallic components are of cubic close-packed structures, it is very likely that the similar atomic close-packed configurations dominate the short-range structure of the BMGs. These highly packed structures have also been confirmed by density measurements. The relative density change of the BMGs between amorphous and fully crystallized states is less than 1.0% [79].

It is worth mentioning that carbon nanotubes are introduced successfully into Zr-based BMGs. The composites with the mixed structure of c-nanotubes and ZrC phase dispersing randomly in the glassy matrix were obtained. The composites is found to have improved mechanical properties relative to the undoped BMGs and excellent wave absorption ability [133]. Fig. 35 shows the ultrasonic velocity and ultrasonic attenuation changes drastically with carbon nanotube addition. It can be seen that the ultrasonic attenuation coefficient increases rapidly with the increase of carbon nanotubes addition. The excellent wave absorption ability of Zr-based BMG composites originates from the random dispersion of residual carbon nanotubes and ZrC phase, the formation of new

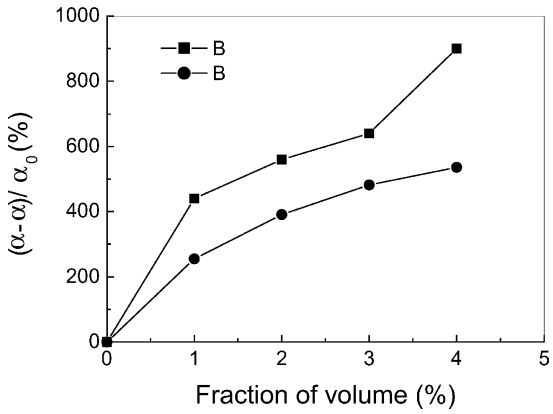

Fig. 35. Relative changes $\Delta\alpha/\alpha_0 = (\alpha - \alpha_0)/\alpha_0$ of variation of the longitudinal and transverse ultrasonic attenuation (α_l and α_t) of Zr-based BMG composites with increasing the volume fractions of carbon nanotube addition (α_0 is attenuation coefficient of the undoped BMG and α is attenuation coefficient of composites) [133].

interfaces, and the denser packed structure in the glass matrix of the composites. The work shows that the composites might have potential of application in the field of shielding acoustic sound or environmental noise.

3.3. Magnetic properties

The BMGs obtained in multicomponent (Nd, Pr)–Fe-based systems have attracted great attention due to their high coercivity and the absence of glass transition before crystallization in isochronal DSC measurements [30,149–153]. The reason for the high coercivity was presumed to be the presence of a relaxed disordered structure that can be regarded as an ensemble of Nd(Pr)–Fe and Nd(Pr)–Fe–Al clusters with large random magnetic anisotropy [150–152]. It seems that this kind of relaxed structure cannot be obtained by the annealing of melt-spun ribbons, because high coercivity was not observed in annealed ribbons. The effect of heavier rare-earth (RE) elements Sm, Dy and Gd substitution for Nd and Pr on the magnetic properties of the $Nd(Pr)_{60}Fe_{30}Al_{10}$ BMG was also studied [154]. However, the RE-rich Sm(Dy, Fe)–Fe-based metallic glasses, in which Sm(Dy, Gd)–Fe clusters may exist, did not show hard magnetic properties at room temperature, irrespective of the quenching rate applied for solidification. Furthermore, the Nd(Pr)-rich Nd–Al–Co, Nd(Pr)–Cu–Ni–Al system displayed paramagnetic properties at room temperature, though the presence of Nd–Co clusters is also possible [37,155]. For Nd-based alloy, it was reported that bulk glass rod with 12 mm in diameter can be obtained by suction casting into a copper mold [148–151]. However, the Nd-based BMG can actually be regarded as a type of clustered amorphous material [98,153,156]. Some direct evidences are that the BMGs have no obvious glass transition in their DSC trace as other BMGs do and exhibits hard magnetic properties while melt-spun ribbons with the same composition are magnetically soft [157]. The mechanisms responsible for the hard magnetic properties of the Nd(Pr)-based BMGs and the relationship between microstructure and magnetic properties are still not clear.

Since 1995, a series of Fe- and Co-based BMGs with ferromagnetism at room temperature has been developed by copper mold casting or water quenching [77,82,158]. The formation and properties of multicomponent Fe-based BMGs have attracted increasing attention because of the fundamental interests in their properties and industrial application potential. The main types of Fe- and Co-based BMGs are [158]: Fe–(Al, Ga)–(P, C, B, Si, Ge); Fe–TM (TM = IV–VIII group

transition metal)–B; Fe(Co)–(Al, Ga)–(P, C, Si, B); Fe–(Co, Ni)–M–B (M = Zr, Hf, Nb, Ta, Mo, W); Fe–Co–Ln–B; Fe–(Nb, Cr, Mo, Ni)–(P, C, B); Co–Fe–(Zr, Hf, Nb)–B soft magnetic BMGs. For the formation of Fe- and Co-based BMGs, the addition method is very effective in improving the GFA and magnetic properties just like in other BMGs [23,77,159–161]. For example, the addition of metalloid and transition metals such as Si, Ge, Nb, Mo, Cr and Co, is effective for the extension of the supercooled liquid region of bulk glass-forming alloys Fe–(Al, Ga)–(P, C, B, Si) BMGs and $(Co_{0.705}Fe_{0.045}Si_{0.10}B_{0.15})_{96}Nb_4$ [160]. The addition of metalloid element Si can increase the saturation magnetization, decrease the coercive force and improve the GFA of $Fe_{77}Ga_3P_{12-x}C_4B_4Si_x$ and $Fe_{78}Ga_2P_{12-x}C_4B_4Si_x$ BMGs [161]. The $Fe_{74}Al_4Sn_2Nb_2P_{10}Si_4B_4$ and $Fe_{61}Co_7Mo_{5-x}Zr_{10}W_2B_{15}Ni_x$ BMGs can be obtained by substitution of Ga with Sn and by partial substitution of Mo with Ni respectively [162]. The $Fe_{61}Co_7Zr_{10}Mo_5W_2M_{15}$ (M = B, Al, Si, C and P) series of alloys were prepared with low purity of raw materials by copper mould cast. The thermal stability of the Fe-based alloy made from low purity raw materials can be much improved by adding a small mount of multi-metalloids [159]. BMGs have much higher GFA so that thicker sheets, plates, larger diameter wires and thick ring can be directly prepared by casting. The maximum diameter of the Fe-based BMG has been reported to reach 5–6 mm.

Compared with the Fe- and Co-based metallic glasses ribbons, the BMGs have the following advantages in soft magnetic properties [77]: (1) high electrical resistivity of 200–250 μΩ cm at room temperature; (2) lower coercive force of 0.2–4 A/m; (3) higher initial permeability; (4) controllable arrangement of domain wall structure achieved by control of casting and/or cooling processes; (5) better high-frequency permeability; (6) good micro-forming ability in supercooled liquid region. On the other hand, the disadvantages of BMGs are: (1) higher materials cost due to the necessity of using special solute elements to obtain an higher GFA; (2) lower saturated magnetic flux density due to the addition of large amount of solute elements, this is a serious obstacle to future use in power transformers. Therefore, a lot of effort is still needed for attaining excellent soft magnetic BMGs. For example, Fig. 36 shows a comparison of *I–H* hysteresis loop of the cast ring-shape Fe-based BMG and similar ring-shape alloy made by stacking the melt-spun ribbons [163]. It can be seen that the bulk ring-shape alloy has a lower coercive force of 2.2 A/m and much higher initial maximum permeability of 110 000 even in the cast state. The subsequent annealing treatment of the ring-shape sample caused a further increase in initial permeability to 180 000 accompanied by a decrease in coercive to 1.0 A/m. The observation of the domain wall structure indicates that the much better soft

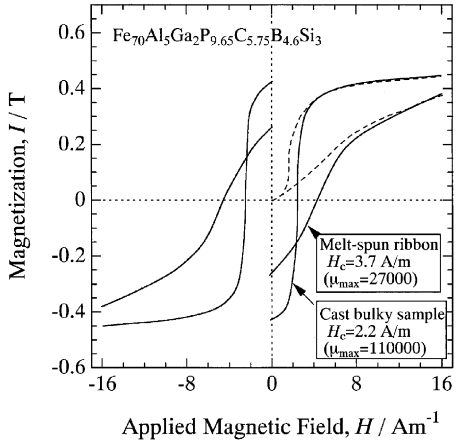

Fig. 36. A comparison of *I–H* hysteresis loop of the cast ring-shape Fe-based BMG and similar ring-shape alloy made by stacking the melt-spun ribbons [163]. (Copyright (2000) by The Japan Institute of Metals.)

magnetic properties for the as-cast ring-shape BMG are due to the well-arrayed domain wall structure aligned in the circumferential direction. The good high-frequency permeability is due to the combination of low coercive resulting from the homogeneous glassy structure and low current loss resulting from high electrical resistivity. It is very likely that further improvements to the soft magnetic properties will allow the practical use of BMGs as soft magnetic materials.

3.4. Other properties and behaviors of BMG under extreme conditions

The investigations of the other physical properties of BMGs are not so extensive compared with the above mentioned properties. Among those, high resistance to corrosion is another excellent properties of BMGs. It is found that even under extremely severe corrosive environment, the BMGs behave passively. P-containing BMGs have the highest corrosion resistance so far, and the Fe-based BMGs' corrosion resistance is good enough to use them as practical corrosion resistant materials [82].

The properties of BMGs under extreme conditions such as low temperature, high pressure, microgravity, etc. are of particular interest. However, up to now, little work has been done in this aspect. Results of superconducting transition temperature measurements were reported for the vit1 and vit4 BMGs before and after annealing [164]. The superconducting critical temperature T_c is 1.84 K for the as-prepared vit4 and 3.76 K for the annealed sample at zero magnetic field, respectively. The temperature gradient $(-dH_{c2}/dT)T_c$ of the upper critical field H_{c2} near the critical temperature T_c of the vit4 is about $2.5T$ (K^{-1}). Annealing of the BMG leads to a decrease of $(-dH_{c2}/dT)T_c$ to $1.2T$ (K^{-1}). The origin of the reduction of the critical temperature T_c in vit4 can be ascribed to a smearing of the density of states by the disordered atomic structure [164].

The low-temperature specific heat C_p of vit1 in the different states were investigated [165]. The results show that the BMG has largest specific heat among the different states, and C_p of the BMG decreases with the extent of crystallization or degree of structural ordering in the alloy. It is found that densities of states at the Fermi level $N(E_F)$ for the glass is highest among the four states they investigated, and it decreases with the structural ordering. The phenomenon is interpreted with reference to localization of electrons in glassy alloys. The value of Debye temperature increases with degree of structural ordering, indicative of marked softening of transverse phonons in the BMG compared with the crystalline states [165].

With more BMG systems developed, one can expect that increasing number of special functional properties of the BMG would be found and this new material will make its way into a variety of other special commercial products.

3.5. Forming and jointing of BMG

Compared with the numerous reports on the alloy compositions and properties, there are relatively few published results on industrial processing of BMGs. In most of the commercially available BMG products, vacuum die-casting is used for producing the desirable shapes of the components. Unlike die-casting of conventional crystalline materials where the flow of molten metal can be improved by heating the mould, die-casting of BMG usually requires faster cooling for retaining the amorphous structure. Therefore, casting of very thin and intricate shapes as well as very large workpieces are difficult. Nevertheless, the casting process is suffix for some applications like casings of personal electronic appliances.

In addition to casting, forming the BMG parts through viscous flow in the supercooled liquid state is also a viable process. The viscous flow behavior of Zr-based BMG was investigated rather

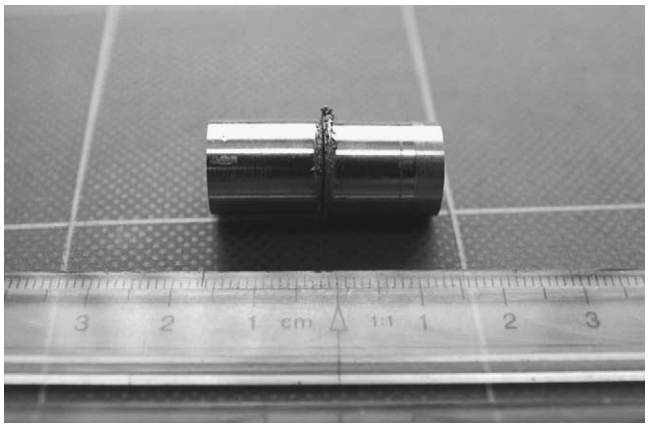

Fig. 37. The appearance of friction-welded bulk metallic glass sample.

extensively [166–171]. The maximum elongation of Zr-based BMG samples under suitable conditions can exceed 300% at a strain rate of 5.0×10^{-2} s^{-1} at 673 K [172] and a value of 10^6% was reported for 5 mm diameter cylindrical specimens [16]. With such high formabilities, not only common small machine components can be fabricated with BMGs, but micromachine components can be made through microforming as well [173]. The alloys at supercooled liquid state behave like a Newtonion fluid and can fill cavities or flow through extrusion dies with sizes in the order of 100 μm.

While the properties of BMGs are attractive for a lot of applications, the limitation of sizes attainable with the material is still constraining the more widespread use of the materials. Furthermore, in order to better integrate the BMG components into the structure of machines or other products, the possibility of joining BMG with BMG or crystalline materials is desirable. The major contribution in this aspect was made by Kawamura et al. [174–178] who demonstrated the success of several welding processes, namely, friction welding, spark welding and electron-beam welding. The major consideration while welding BMGs is whether the glassy state can be retained after the processes, which usually involve the supply of heat for softening the metallic glasses. Their results and those by Wong and Shek [179] (Fig. 37) confirm that with careful control of the process parameters, the joints remain amorphous and the strength is comparable to the bulk of the metallic glass.

4. Potential applications

With the unique and unconventional characteristics, BMG materials are adopted for application in various fields. One of the great advantages of BMGs is the ease of formation of complicated shapes. Up to now, BMGs have already been used as die materials (Pd–Cu–Ni–P BMG), sporting equipment (ZrTiCuNiBe and ZrTiNiCu BMGs) and electrode materials (PdCuSiP BMG). The development of Fe-based BMGs has reached the final stage for application as soft magnetic materials for common mode choke coils. Success in this area will result in the increasing importance of BMGs in engineering. Table 8 summarizes the present and future application potentials for the BMGs.

The first step of the new family of materials into the market is the application for making golf plate [11]. In addition to the merits like low density and high strength-to-weight ratio, other

Table 8
Possible application fields for BMGs

Properties	Application field
High strength	Machinery structural materials
High hardness	Cutting materials
High fracture toughness	Die materials
High impact fracture energy	Tool materials
High fatigue strength	Bonding materials
High elastic energy	Sporting goods materials
High corrosion resistance	Corrosion resistance materials
High wear resistance	Writing appliance materials
High reflection ratio	Optical precision materials
High hydrogen storage	Hydrogen storage materials
Good soft magnetism	Soft magnetic materials
High frequency permeability	High magnetostrictive materials
Efficient electrode	Electrode materials
High viscous flowability	Composite materials
High acoustic attenuation	Acoustic absorption materials
Self-sharping property	Penetrator
High wear resistance and manufacturability	Medical devices materials

properties such as low elastic modulus and lower vibrational response provide a softer, more solid feel for better control when a golfer strikes the ball. The negligible hysteresis loss of BMG means that less energy is absorbed by the club head at impact, so more energy is transferred to the ball. According to the literature of the BMG golf plate manufacturer [180], steel club heads transfer about 60% of the input energy to the ball and titanium transfers 70%, whereas the metallic glass transfers 99%. With such favorable properties, BMGs are also applied in other high-end sporting goods such as tennis rackets, and may also find applications for baseball bats, bicycle frames, hunting bows, and even edged tools such as axes. A newly developed application utilizing the efficient energy transfer characteristics is the use of BMG spheres for shot-peening purpose [181]. On the other hand, the possibility of moulding into components with thin sections allows BMG to challenge magnesium alloys in the electronic appliances market. With the trend of miniaturization of personal electronic devices such as MP3 players and personal digital assistants (PDA), there is a pressing need to make the casing thinner while retaining sufficient mechanical strength. BMGs exhibit obvious advantages over polymeric materials and conventional light alloys. Mobile phones and digital still cameras with BMG casing are already developed [180].

In addition to sporting goods, the new family of materials could also be promising for other more serious applications. Under a contract from the US Army Research Office, for example, researchers in USA are working to develop manufacturing technology for metallic-glass tank-armor penetrator rounds to replace the current depleted uranium penetrators, which are suspected of biological toxicity. The tungsten composite penetrator exhibits self-sharpening behavior similar to that of oxide glasses and is highly efficient in piercing armor plates. Applications in military context are usually among the most stringent and demanding classes. High reliability combined with mobility are the key requirements. The high strength and light weight of BMG allows miniaturization and weight reduction in the designs of military components without sacrificing the reliability. Examples are sub-munition components, thin walled casings and components for electronics, aircraft fasteners, etc. [180].

Another area of commercial interest is a highly biocompatible, non-allergic form of the glassy material that would be suitable for medical components such as prosthetic implants and surgical instruments. The unique properties of BMGs for orthopedic applications include: (1) biocompatible;

(2) excellent wear resistance; (3) high strength-to-weight ratio compared to titanium and/or stainless steel; (4) more than twice the strength compared to titanium or stainless steel; (5) possibility of precision net-shape casting with desirable surface texture which results in significant reduction in post-processing. Some of the products taking advantage of these improvements include reconstructive devices, fractured fixations, spinal implants and instrumentation. Another opportunity for medical applications is in the field of ophthalmic surgery, where procedures and instruments are being enhanced to better serve patients in need of cataract surgery [180].

NASA's Genesis spacecraft, the first mission to collect and return samples of the solar wind—fast moving particles from the Sun—will help scientists refine the basic definition of the Sun's characteristics, and understand how the solar nebula, a large cloud of gas and dust, gave rise to our complex solar system. Genesis has received its final piece of science equipment: a solar wind collector made of a new formula of bulk metallic glass. This metallic glass collector and other solar wind collector tiles on the spacecraft will collect the first-ever samples of the solar wind as the spacecraft floats in the oncoming solar stream. Genesis will have collected elements of the solar wind such as isotopes of oxygen and nitrogen. Bringing back samples of the solar wind will provide the next century of scientists with a databank of solar composition, a disk made of a unique formulation of bulk metallic glass created especially for Genesis. The shaft on which the plates rotate is capped with the disk of the BMG. The Genesis metallic glass was prepared in a collaborative effort by the Howmet Corporation. The surfaces of metallic glasses dissolve evenly, allowing the captured ions to be released in equal layers by sophisticated acid etching techniques. One exciting thing about BMG is that it will enable us to study ions with energies higher than the solar wind. This allows Genesis to test proposals that the higher energy particles differ in composition from the solar wind. This will be the first time the theories about different kinds of solar wind can be tested by bringing back actual samples.

One of the latest industries attracted by the BMG is the fine jewelry industry. The BMGs can achieve a stunning surface finish which catches the attention of high-end jewelry makers worldwide. The high-performance characteristics and unique properties of BMG can create a metal surface that is both exceptionally hard and scratch resistant, but can be polished to a high luster that is maintained over time. Also, the ability of BMGs to be precision net-shape cast enables jewelry designers to create bold lines and sensual, unique shapes not easily achieved with traditional metals.

In the near future, BMGs materials will become more and more significant for basic research and applications as the science and technology of this new field undergo further development.

Acknowledgements

The authors are grateful for the financial support of the National Natural Science Foundation of China (Grant numbers: 59925101 and 50031010), Chinesisch-Deutsches Zentrum Fuer Wissenschaftsfoerderung (Grant no.: GZ032/7) and the Key Project of the Beijing Science and Technology Program (Contract no.: H02040030320). One of the authors (WHW) thanks the contribution to the paper by all his group members in Institute of Physics, CAS.

References

[1] W. Clement, R.H. Willens, P. Duwez, Nature 187 (1960) 869.
[2] A.L. Greer, Science 267 (1995) 1947.

[3] W.L. Johnson, Prog. Mater. Sci. 30 (1986) 81.
[4] H.A. Daveis, in: F.E. Luborsky (Ed.), Amorphous Metallic Alloys, Butterworths, London, 1983, p. 8.
[5] S. Kavesh, in: J.J. Gillman, H.L. Leamy (Eds.), Metallic Glasses, ASM International, Metals Park, OH, 1978 (Chapter 2).
[6] D. Turnbull, Trans. AIME 221 (1961) 422.
[7] H.S. Chen, D. Turnbull, J. Chem. Phys. 48 (1968) 2560.
[8] H.S. Chen, D. Turnbull, Acta Metall. 17 (1969) 1021.
[9] D. Turnbull, J.C. Fisher, J. Chem. Phys. 17 (1949) 71.
[10] D. Turnbull, Contemp. Phys. 10 (1969) 437.
[11] W.L. Johnson, MRS Bull. 24 (10) (1999) 42.
[12] H.S. Chen, Acta Metall. 22 (1974) 1505.
[13] A.L. Drehman, A.L. Greer, D. Turnbull, Appl. Phys. Lett. 41 (1982) 716.
[14] W.H. Kui, A.L. Greer, D. Turnbull, Appl. Phys. Lett. 45 (1984) 615.
[15] A. Inoue, T. Zhang, T. Masumoto, Mater. Trans. JIM 30 (1989) 965.
[16] A. Inoue, Acta Mater. 48 (2000) 279.
[17] A. Inoue, T. Nakamura, N. Nishiyama, T. Masumoto, Mater. Trans. JIM 33 (1992) 937.
[18] A. Inoue, Mater. Trans. JIM 36 (1995) 866.
[19] A. Inoue, T. Zhang, T. Masumoto, Mater. Trans. JIM 34 (1993) 1234.
[20] A. Peker, W.L. Johnson, Appl. Phys. Lett. 63 (1993) 2342.
[21] A. Inoue, N. Nishiyama, Mater. Sci. Eng. A 226–228 (1997) 401.
[22] A. Inoue, T. Zhang, H. Koshiba, A. Makino, J. Appl. Phys. 83 (1998) 6326–6328.
[23] W.H. Wang, Z. Bian, P. Wen, D.Q. Zhao, Intermetallic 10 (2002) 1249;
W.H. Wang, Q. Wei, H.Y. Bai, Appl. Phys. Lett. 71 (1997) 58.
[24] C.T. Liu, M.F. Chisholm, M.K. Miller, Intermetallic 10 (2002) 1105.
[25] H. Choi-Yim, R. Busch, U. Koster, W.L. Johnson, Acta Mater. 47 (1999) 2455.
[26] R.D. Conner, H. Choi-Yim, W.L. Johnson, J. Mater. Res. 14 (1999) 3292.
[27] C.C. Hays, C.P. Kim, W.L. Johnson, Phys. Rev. Lett. 84 (2000) 2901.
[28] W.H. Wang, R.J. Wang, J. Eckert, Mater. Trans. JIM 42 (2001) 587.
[29] H.S. Chen, J.T. Krause, E. Coleman, J. Non-Cryst. Solids 18 (1975) 157.
[30] Y. He, C.E. Price, S.J. Poon, Phil. Mag. Lett. 70 (1994) 371.
[31] X.H. Lin, W.L. Johnson, J. Appl. Phys. 78 (1995) 6514.
[32] H. Tan, Z.P. Lu, H.B. Yao, Y. Li, Mater. Trans. JIM 42 (2001) 551.
[33] M. Leonhardt, W. Loeser, H.G. Lindenkreuz, Acta Mater. 47 (1999) 2961.
[34] Y. Zhang, D.Q. Zhao, B.C. Wei, P. Wen, M.X. Pan, W.H. Wang, J. Mater. Res. 16 (2001) 1675.
[35] S.J. Poon, G.J. Shiflet, V. Ponnambalam, V.M. Keppens, R. Taylor, G. Petculescu, Mater. Res. Soc. Symp. Proc. 754 (2003) CC1.2.1.
[36] H. Choi-Yim, D. Xu, W.L. Johnson, Appl. Phys. Lett. 82 (2003) 1030.
[37] Z.F. Zhao, Z. Zhang, P. Wen, M.X. Pan, D.Q. Zhao, W.H. Wang, Appl. Phys. Lett. 82 (2003) 4699.
[38] A.L. Greer, Nature 366 (1993) 303.
[39] A. Inoue, Mater. Trans. JIM 36 (1995) 866.
[40] R. Busch, Y.J. Kim, W.L. Johnson, J. Appl. Phys. 77 (1995) 4039.
[41] R. Busch, W. Liu, W.L. Johnson, J. Appl. Phys. 83 (1998) 4134.
[42] L.E. Tanner, Acta Metall. 27 (1979) 1727.
[43] A. Peker, Ph.D. Dissertation, California Institute of Technology, 1994.
[44] Z.P. Lu, C.T. Liu, Acta Mater. 50 (2002) 3501–3512.
[45] R. Busch, JOM 52 (7) (2000) 39.
[46] J. Eckert, JOM 52 (7) (2000) 43.
[47] R. Busch, E. Bake, W.L. Johnson, Acta Mater. 46 (1998) 4725.
[48] E. Bakke, R. Busch, W.L. Johnson, Appl. Phys. Lett. 67 (1995) 3260.
[49] A. Angell, Science 267 (1995) 1924.
[50] H. Tanaka, Phys. Rev. Lett. 90 (2003) 557011.
[51] A. Meyer, Phys. Rev. lett. 80 (1998) 4454.
[52] A. Meyer, R. Busch, H. Schober, Phys. Rev. Lett. 85 (1999) 5027.
[53] U. Geyer, S. Schneider, W.L. Johnson, Y. Qiu, T.A. Tombrello, M.-P. Macht, Phys. Rev. Lett. 75 (1995) 2364.
[54] X.-P. Tang, R. Busch, W.L. Johnson, Y. Wu, Phys. Rev. Lett. 81 (1998) 5358.
[55] X.-P. Tang, U. Geyer, R. Busch, W.L. Johnson, Y. Wu, Nature 402 (1999) 160.
[56] S.R. Nagel, J. Tauc, Phys. Rev. Lett. 35 (1975) 380.
[57] S.R. Nagel, Phys. Rev. B 16 (1977) 1694.
[58] S.R. Nagel, J. Vassiliou, P.M. Horn, B.C. Giessen, Phys. Rev. B 17 (1978) 46.
[59] H. Beck, R. Oberle, in: B. Cantor (Ed.), Proceedings of the Third International Conference on Rapidly Quenched Metals, University of Sussex, UK, 1978, p. 416.

[60] P. Häussler, J. Krieg, G. Indlekofer, P. Oelhafen, H.-J. Güntherodt, Phys. Rev. Lett. 41 (1983) 714.
[61] P. Haussler, Phys. Rep. 222 (2) (1992) 65.
[62] U. Mizutani, Prog. Mater. Sci. 28 (1983) 97.
[63] U. Mizutani, K.T. Hartwig, T.B. Massalski, R.W. Hopper, Phys. Rev. Lett. 41 (1978) 661.
[64] U. Mizutani, K. Yashino, J. Phys. F14 (1984) 1179.
[65] T. Fujiwara, T. Yokokawa, Phys. Rev. Lett. 66 (1991) 333.
[66] J. Hafner, M. Krajci, Phys. Rev. B 47 (1993) 11795.
[67] D. Mayou, F. Cyrot-Lackmann, G. Trambly de Laissardiére, T. Klein, J. Non-Cryst. Solids 153/154 (1993) 412.
[68] G. Trambly de Laissardiére, D. Nguyen Manh, L. Magaud, J.P. Julien, F. Cyrot-Lackmann, D. Mayou, Phys. Rev. B 52 (1995) 7920.
[69] U. Mizutani, T. Takeuchi, H. Sato, Prog. Mater. Sci. 49 (2004) 227–261.
[70] J. Friedel, Helv. Phys. Acta 61 (1988) 538.
[71] Y.M. Wang, J.B. Qiang, C.H. Wong, C.H. Shek, C. Dong, J. Mater. Res. 18 (2003) 642.
[72] A. Inoue, T. Zhang, T. Masumoto, Mater. Trans. JIM 31 (1990) 177.
[73] Y.M. Wang, X.F. Zhang, J.B. Qiang, Q. Wang, D.H. Wang, D.J. Li, C.H. Shek, C. Dong, Scripta Mater. 50 (2004) 829–833.
[74] Y.M. Wang, C.H. Shek, J.B. Qiang, C.H. Wong, Q. Wang, X.F. Zhang, C. Dong, The *e/a* criterion for the largest glass-forming abilities of the Zr–Al–Ni(Co) alloys, Mater. Trans., in press.
[75] W.R. Chen, Y.M. Wang, J.B. Qiang, C. Dong, Acta Mater. 51 (7) (2003) 1899.
[76] A. Inoue, T. Zhang, N. Nishiyama, K. Ohba, T. Masumoto, Mater. Trans. JIM 34 (1993) 1234.
[77] A. Inoue, A. Takeuchi, Mater. Trans. JIM 43 (2002) 1892.
[78] A. Inoue, A.R. Yavari, Mater. Trans. JIM 39 (1998) 318.
[79] W.H. Wang, L.L. Li, R.J. Wang, Phys. Rev. B 62 (2001) 11292.
[80] W.H. Wang, Q. Wei, M.P. Macht, H. Wollenberger, Appl. Phys. Lett. 71 (1997) 1053.
[81] W.H. Wang, Q. Wei, S. Friedrich, Phys. Rev. B 57 (1998) 8211.
[82] A. Inoue, Bulk Amorphous Alloys, Tans Tech Publications, Zurich, 1998.
[83] J. Eckert, N. Mattern, M. Seidel, Mater. Trans. JIM 39 (1998) 623.
[84] W.H. Wang, E. Wu, R.J. Wang, A.J. Studer, Phys. Rev. B 66 (2002) 104205.
[85] J. Saida, M. Matsushita, A. Inoue, Appl. Phys. Lett. 79 (2001) 412.
[86] T.A. Waniuk, J. Schroers, W.L. Johnson, Phys. Rev. B 67 (2003) 184203.
[87] D. Holland-Moritz, Phys. Rev. Lett. 71 (1993) 1196.
[88] R. Wang, Nature 278 (1979) 700.
[89] J. Schroers, W.L. Johnson, Appl. Phys. Lett. 76 (2000) 2343.
[90] J. Schroers, W.L. Johnson, J. Appl. Phys. 88 (2000) 44.
[91] J. Schroers, A. Masuhr, W.L. Johnson, R. Busch, Phys. Rev. B 60 (1999) 11855.
[92] J. Schroers, R. Busch, A. Masuhr, W.L. Johnson, Appl. Phys. Lett. 74 (1999) 2806.
[93] T.A. Waniuk, J. Schroers, W.L. Johnson, Appl. Phys. Lett. 78 (2001) 1213.
[94] J. Schroers, Y. Wu, R. Busch, W.L. Johnson, Acta Mater. 49 (2001) 2773.
[95] W.H. Wang, J. Metastable Nano-Cryst. Mater. 15/16 (2003) 73.
[96] W.H. Wang, D.W. He, D.Q. Zhao, Y.S. Yao, Appl. Phys. Lett. 75 (1999) 2770.
[97] W.H. Wang, Y.X. Zhuang, M.X. Pan, Y.S. Yao, J. Appl. Phys. 88 (2000) 3914.
[98] Z. Zhang, W.H. Wang, Appl. Phys. Lett. 81 (2002) 4371.
[99] J.-J. Kim, Y. Choi, S. Suresh, A.S. Argon, Science 295 (2002) 654.
[100] J. Zhang, K.Q. Qiu, H.F. Zhang, Z.Q. Hu, J. Mater. Res. 17 (2002) 2935.
[101] A. Gebert, J. Ekert, L. Schultz, Acta Mater. 46 (1998) 5475.
[102] M. Yousuf, K.G. Rajan, J. Mater. Sci. Lett. 3 (1984) 149.
[103] Z.Y. Shen, G.Y. Chen, Y. Zhang, X.J. Yin, Phys. Rev. B 39 (1989) 2714.
[104] W.K. Wang, H. Iwasaki, K. Fukamichi, J. Mater. Sci. 15 (1980) 2701.
[105] W.H. Wang, T. Okada, W. Utsumi, Unpublished.
[106] J.Z. Jiang, Y.X. Zhuang, J. Saida, A. Inoue, Phys. Rev. B 64 (2001) 094208.
[107] J.Z. Jiang, K. Saksi, H. Rasmussen, Appl. Phys. Lett. 79 (2001) 1112.
[108] W.K. Wang, H. Iwasaki, T. Masumoto, J. Mater. Sci. 8 (1982) 3765.
[109] F. He, K. Lu, Acta Mater. 47 (1999) 2449.
[110] W.H. Wang, R.J. Wang, M.X. Pan, Y.S. Yao, Appl. Phys. Lett. 79 (2001) 1106.
[111] A. Inoue, W. Zhang, T. Zhang, K. Kurosaka, Acta Mater. 49 (2001) 2645.
[112] A. Inoue, T. Zhang, K. Kurosaka, Appl. Phys. Lett. 71 (1997) 464.
[113] W.H. Wang, R.J. Wang, D.Q. Zhao, M.X. Pan, Appl. Phys. Lett. 74 (1999) 1803.
[114] C.A. Schuh, T.G. Nieh, Y. Kawamura, J. Mater. Res. 17 (2002) 1651.
[115] C.A. Schuh, T.G. Nieh, Acta Mater. 51 (2003) 87.
[116] C.C. Hays, C.P. Kim, W.L. Johnson, Phys. Rev. Lett. 84 (2000) 2901.

[117] J. Xu, M.H. Manghnani, Phys. Rev. B 45 (1992) 640.
[118] R.C. Purdom, E.W. Prohofsky, Phys. Rev. B 2 (1970) 551.
[119] M. Grimsditch, K.E. Gray, R. Bhadra, L.E. Rehn, Phys. Rev. B 35 (1987) 883.
[120] P.W. Bridgman, Proc. Am. Acad. Arts Sci. 74 (1942) 425.
[121] P. Wen, R.J. Wang, M.X. Pan, D.Q. Zhao, W.H. Wang, J. Appl. Phys. 93 (2003) 759.
[122] Y. Zhang, Y.F. Ji, D.Q. Zhao, Y.X. Zhuang, R.J. Wang, M.X. Pan, Y.D. Dong, W.H. Wang, Scripta Mater. 44 (2001) 1107.
[123] Y. Zhang, D.Q. Zhao, R.J. Wang, W.H. Wang, Acta Mater. 51 (2003) 1971.
[124] W.H. Wang, H.Y. Bai, J.L. Luo, R.J. Wang, D. Jin, Phys. Rev. B 62 (2000) 25.
[125] L.M. Wang, W.H. Wang, R.J. Wang, Z.J. Zhan, D.Y. Dai, L.L. Sun, W.K. Wang, Appl. Phys. Lett. 77 (2000) 1147.
[126] L.M. Wang, L.L. Sun, W.H. Wang, W.K. Wang, Appl. Phys. Lett. 77 (2000) 3734.
[127] W.H. Wang, P. Wen, Y. Zhang, M.X. Pan, R.J. Wang, Appl. Phys. Lett. 79 (2001) 3947.
[128] W.H. Wang, R.J. Wang, W.T. Yang, B.C. Wei, P. Wen, D.Q. Zhao, M.X. Pan, J. Mater. Res. 17 (6) (2002) 1385.
[129] P. Wen, R.J. Wang, W.H. Wang, J. Mater. Res. 17 (2002) 1785.
[130] R.J. Wang, F.Y. Li, W.H. Wang, Z.C. Qin, J. Phys. Condens. Matter 14 (2002) 11311.
[131] L.M. Wang, R.J. Wang, W.H. Wang, W.K. Wang, J. Phys. C 15 (2003) 101.
[132] R.J. Wang, W.H. Wang, F.Y. Li, L.M. Wang, J. Phys. C 15 (2003) 603.
[133] Z. Bian, R.J. Wang, M.X. Pan, D.Q. Zhao, W.H. Wang, Adv. Mater. 15 (2003) 616.
[134] Z. Zhang, R.J. Wang, M.X. Pan, W.H. Wang, J. Phys. C 15 (2003) 4503.
[135] D. Schreiber, Elastic Constants and their Measurement, McGraw-Hill, New York, 1973.
[136] D.E. Gray, American Institute of Physics Handbook, 3rd ed., McGraw-Hill, New York, 1973 (Chapter 3).
[137] H.S. Chen, J.T. Krause, E. Coleman, J. Non-Cryst. Solids 18 (1975) 157.
[138] R. Zallen, The Physics of Amorphous Solids, Wiley/Interscience, New York, 1983.
[139] G.A. Saunder, D. Ball, M. Cankurtaran, Q. Wang, E. Amscheidt, C. Jacobs, F. Imbierwitz, J. Pelzl, H. Bach, Phys. Rev. B 55 (1997) 11181.
[140] O.L. Anderson, J. Geophys. Res. 73 (1968) 5187.
[141] F.P. Mallinder, B.A. Proctor, Phys. Chem. Glasses 5 (1964) 91.
[142] B.E. Powell, M.J. Skove, Phys. Rev. 174 (1968) 977.
[143] H.H. Barrett, M.G. Holland, Phys. Rev. B 1 (1970) 2538.
[144] C. Kittel, Introduction to Solid State Physics, 6th ed., Wiley, New York, 1986.
[145] S.S. Bhatli, S.T. Singh, J. Pure Appl. Ultrason. 8 (1986) 101.
[146] F.D. Murnaghan, Proc. Natl. Acad. Sci. U.S.A. 30 (1944) 244.
[147] W.H. Wang, Z.X. Bao, Phys. Rev. B 61 (2000) 3166.
[148] P.W. Bridgman, The Physics of High Pressure, Bell and Sons, London, 1958.
[149] Y. Li, S.C. Ng, Z.P. Lu, Y.P. Feng, K. Lu, Phil. Mag. Lett. 78 (1998) 213.
[150] L.Q. Xing, J. Eckert, W. Löser, L. Schultz, J. Appl. Phys. 88 (2000) 3565.
[151] A. Inoue, T. Zhang, A. Takeuchi, W. Zhang, Mater. Trans. JIM 37 (1996) 636.
[152] B.C. Wei, W.H. Wang, M.X. Pan, B.S. Han, Phys. Rev. B 64 (2001) 012406.
[153] B.C. Wei, W. Löser, W.H. Wang, J. Eckert, Acta Mater. 50 (2002) 4357.
[154] G.J. Fan, W. Löser, S. Roth, J. Eckert, Acta Mater. 48 (2000) 3823.
[155] Z. Zhang, W.H. Wang, Unpublished.
[156] L. Xia, B.C. Wei, M.X. Pan, D.Q. Zhao, W.H. Wang, Y.D. Dong, J. Phys. Condens. Matter 15 (2003) 3531.
[157] B.C. Wei, D.Q. Zhao, W.H. Wang, J. Appl. Phys. 89 (2001) 3529.
[158] A. Inoue, A. Takeuchi, Mater. Sci. Forum 262 (1998) 855.
[159] Y. Hu, M.X. Pan, L. Liu, W.H. Wang, Mater. Lett. 57 (2003) 2698.
[160] A. Inoue, A. Murakami, A. Takeuchi, Mater. Trans. JIM 38 (1997) 189.
[161] B.L. Shen, A. Inoue, Mater. Trans. 43 (2002) 1235.
[162] M.X. Pan, Y. Hu, W.H. Wang, J. Metastable Nano-Cryst. Mater. 15/16 (2003) 99.
[163] A. Makino, A. Inoue, Mater. Trans. JIM 41 (2000) 1471.
[164] Y. Li, H.Y. Bai, P. Wen, Z.X. Liu, Z.F. Zhao, J. Phys. Condens. Matter 15 (2003) 4809.
[165] H.Y. Bai, J.L. Luo, J. Zhang, Z.J. Chen, J. Appl. Phys. 91 (2002) 9123.
[166] T.A. Waniuk, R. Busch, A. Masuhr, W.L. Johnson, Acta Mater. 46 (1998) 5229–5236.
[167] Y. Kawamura, T. Shibata, A. Inoue, T. Masumoto, Appl. Phys. Lett. 69 (1996) 1208.
[168] Y. Kawamura, T. Shibata, A. Inoue, T. Masumoto, Appl. Phys. Lett. 71 (1997) 779.
[169] Y. Kawamura, T. Shibata, A. Inoue, T. Masumoto, Scripta Metall. Mater. 37 (1997) 431.
[170] Y. Kawamura, T. Shibata, A. Inoue, T. Masumoto, Acta Mater. 46 (1) (1998) 253–263.
[171] W.N. Myung, S.P. Ryu, I.S. Hwang, H.G. Kim, T. Zhang, A. Inoue, A.L. Greer, Mater. Sci. Eng. A 304–306 (2001) 691–695.
[172] Y. Kawamura, T. Shibata, A. Inoue, T. Masumoto, Scripta Mater. 37 (4) (1997) 431–436.

[173] Y. Saotome, T. Zhang, A. Inoue, Mater. Res. Soc. Symp. Proc. 554 (1999) 385–390.
[174] Y. Kawamura, Y. Ohno, Scripta Mater. 45 (2001) 127–132.
[175] Y. Kawamura, Y. Ohno, Scripta Mater. 45 (2001) 279–285.
[176] Y. Kawamura, Y. Ohno, Mater. Trans. 42 (11) (2001) 2476–2478.
[177] Y. Kawamura, S. Kagao, Y. Ohno, Mater. Trans. 42 (12) (2001) 2649–2651.
[178] Y. Kawamura, T. Shoji, Y. Ohno, J. Non-Cryst. Solids 317 (1–2) (2003) 152–157.
[179] C.H. Wong, C.H. Shek, Scripta Mater. 49 (2003) 393–397.
[180] http://www.liquidmetal.com.
[181] A. Inoue, B.L. Shen, W. Zhang, in: Proceedings of the Third International Conference on Bulk Metallic Glasses, Beijing, October 2003.